Accepted Manuscript

3D nano-architected metallic glass: Size effect suppresses catastrophic failure

Rachel Liontas, Julia R. Greer

Please cite this article as: R. Liontas, J.R. Greer, 3D nano-architected metallic glass: Size effect suppresses catastrophic failure, *Acta Materialia* (2017), doi: 10.1016/j.actamat.2017.05.019.
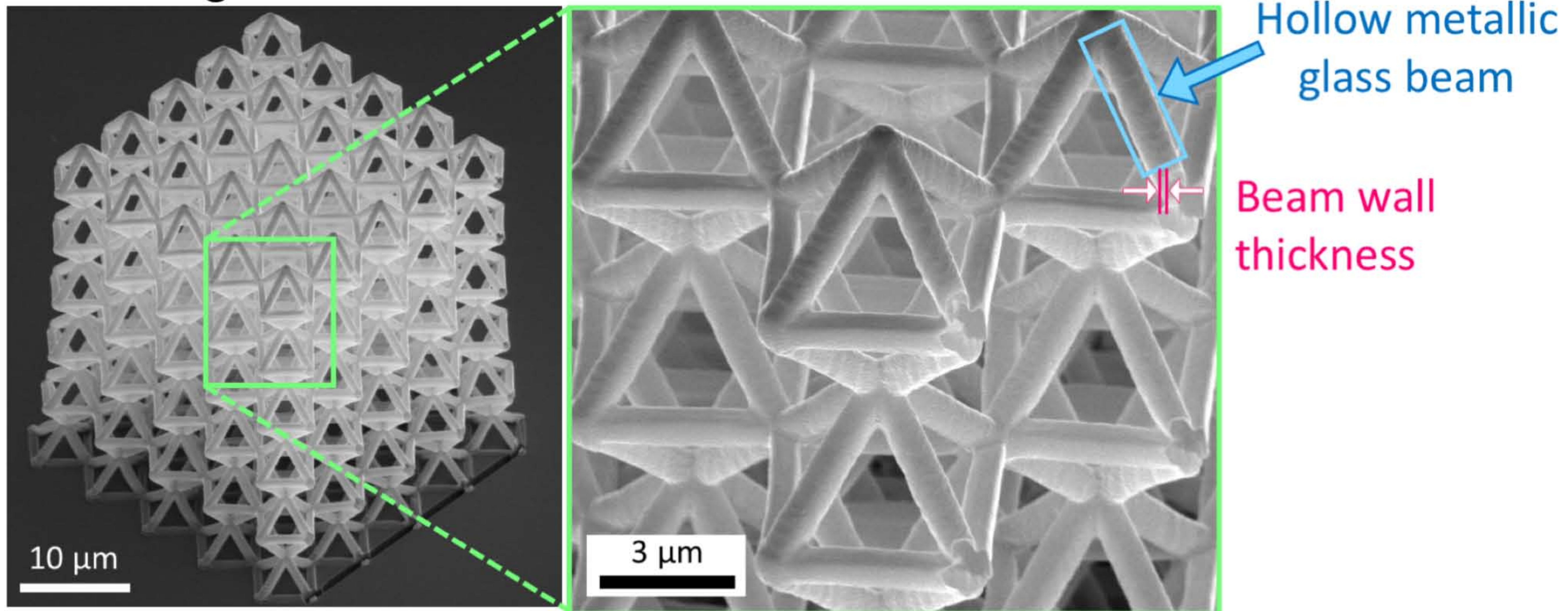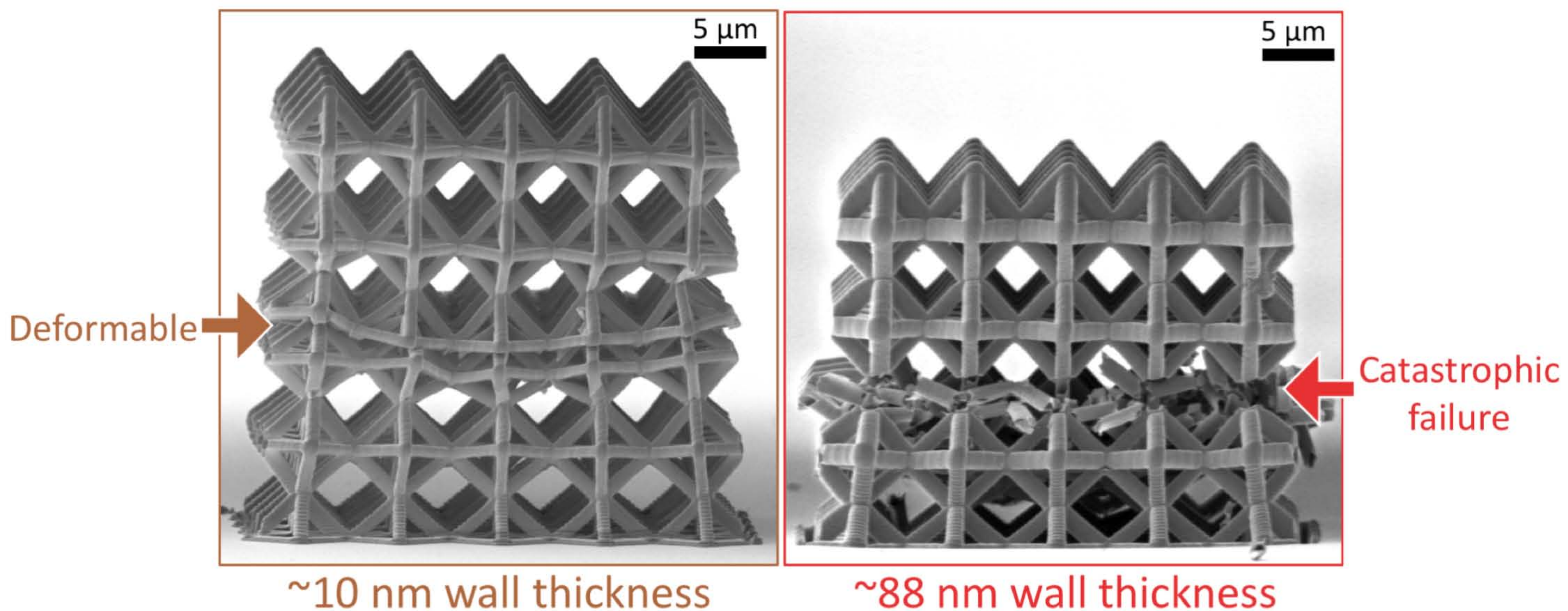
Metallic glass nanolattice

Hollow metallic glass beam

Beam wall thickness

10 μm

3 μm

After compression to ~33% strain

5 μm

5 μm

Deformable

Catastrophic failure
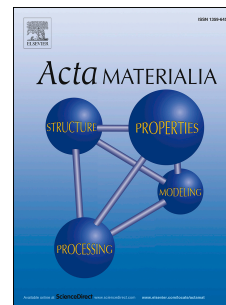
~10 nm wall thickness

~88 nm wall thickness

Deformability in hollow metallic glass nanolattices is achieved by decreasing the wall thickness of the nanolattice beams. Nano-architecting in this way enables the "smaller is more deformable" material size effect first observed in metallic glasses nanopillars to be proliferated to larger nanolattice structures as long as the characteristic nanolattice dimension, the wall thickness, is kept below a critical value ~50 nm.

3D nano-architected metallic glass: size effect suppresses catastrophic failure

Rachel Liontas[a] and Julia R. Greer[b]*

[a] Division of Chemistry and Chemical Engineering, California Institute of Technology, Pasadena, CA 91125, USA
[b] Division of Engineering and Applied Science, California Institute of Technology, Pasadena, CA 91125, USA
*Corresponding author. Email address: jrgreer@caltech.edu

Abstract

We investigate the mechanical behavior of 3D periodically architected metallic glass nanolattices, constructed from hollow beams of sputtered Zr-Ni-Al metallic glass. Nanolattices composed of beams with different wall thicknesses are fabricated by varying the sputter deposition time, resulting in nanolattices with median wall thicknesses of ~88 nm, ~57 nm, ~38 nm, ~30 nm, ~20 nm, and ~10 nm. Uniaxial compression experiments conducted inside a scanning electron microscope reveal a transition from brittle, catastrophic failure in thicker-walled nanolattices (median wall thicknesses of ~88 and ~57 nm) to deformable, gradual, layer-by-layer collapse in thinner-walled nanolattices (median wall thicknesses of ~38 nm and less). As the nanolattice wall thickness is varied, large differences in deformability are manifested through the severity of strain bursts, nanolattice recovery after compression, and in-situ images obtained during compression experiments. We explain the brittle-to-deformable transition that occurs as the nanolattice wall thickness decreases in terms of the "smaller is more deformable" material size effect that arises in nano-sized metallic glasses. This work demonstrates that the nano-induced failure-suppression size effect that emerges in small-scale metallic glasses can be proliferated to larger-scale materials by the virtue of architecting.

1. Introduction

Metallic glasses are a class of materials that offer beneficial mechanical properties such as high strength and a large elastic strain limit [1,2]. The lack of grain boundaries in metallic glasses leads to excellent corrosion and wear resistance as well as great soft magnetic properties [1-3]. Despite these desirable properties, metallic glasses have seen limited use in applications owing to their low ductility and characteristic catastrophic failure. Room temperature deformation of metallic glasses typically involves localization of plastic strain into narrow shear bands [4]. Studies have found that this catastrophic failure can be alleviated by reducing the sample size of metallic glass to the nanoscale, where a size-induced brittle-to-ductile transition occurs, observed under both compression [5-7] and tension [8-10]. Tensile ductility at room temperature in metallic glasses is particularly elusive, and has only been shown to emerge in monolithic metallic glasses when the sample size is reduced to these nanoscale dimensions. Previous studies have found that ~100 nm diameter metallic glass pillars can reach true tensile strains of ~25% prior to failure [8,9], and our previous work demonstrated that sputtered Zr-Ni-Al metallic glass nanopillars can reach true strains of ~150% for sample widths up to ~150 nm [11]. These studies show that reducing the characteristic dimension of metallic glass to the nano-scale can alleviate metallic glasses' Achilles' heel of brittle failure, thereby enabling the use of metallic glasses without catastrophic failure.

Advances in small-scale technological devices such as MEMS (microelectromechanical systems), biomedical devices and implants, microelectronics, micromanipulators, and microrobotics have increased the demand for miniature parts fabricated from materials with suitable properties [12,13]. The combination of metallic glasses' enhanced plasticity at small scales [5-11] with their other desirable properties (including high elasticity, an

isotropic/homogeneous nature, and excellent corrosion/wear resistance) [1,2] points towards metallic glasses as promising candidates for use in such small-scale technological devices. Fabricating metallic glasses as thin films, for example by sputtering, presents a unique opportunity to create very thin coatings that may more readily benefit from the size-induced brittle-to-ductile transition in metallic glasses. The use of thin film deposition also interfaces well with existing micro- and nano- fabrication techniques utilized in creating small-scale technological devices. Thin films can be extended to 3-dimensions by "wrapping" the thin film around some 3-dimensional architecture.

Large deformable metallic glasses may be envisioned through nano-architecting, that is maintaining a key dimension of the metallic glass (such as the thin film thickness) at the nanoscale without limiting the overall macroscopic dimensions of the architecture. We utilize this nano-architecting approach by fabricating hollow metallic glass nanolattices with the beam wall thickness in the "smaller is more deformable" nanoscale size range, while the entire nanolattice structure spans tens of microns. These nanolattices can be made arbitrarily large when experimental practicalities are neglected. We chose to work with sputter-deposited Zr-Ni-Al as the thin film metallic glass "coating" for the nanolattices based on this material's substantial tensile ductility at dimensions up to ~150 nm [11].

Nanolattices, or architected structural metamaterials, exhibit hierarchical ordering ranging from nanometer length scales in wall thickness to micron length scales in defining unit cells and beyond millimeter scales in the overall macroscale architecture, with many nano-architectures produced by using direct-laser-writing two-photon lithography [14-17]. Existing work on nanolattices has primarily focused on hollow ceramic nanolattices [18-22], due to the ease of depositing conformal coatings of ceramic materials by atomic layer deposition (ALD) and the

inertness of these ceramic materials to oxygen plasma, which has thus far been the plasma of choice for etching away the internal polymer scaffold to produce nanolattices. One of the key findings from these studies is that by optimizing the wall thickness-to-radius ratio of the nanolattice beams, hollow alumina nanolattices can recover to their original shape after compression in excess of 50% strain [20]. There have also been a few studies on hollow Au nanolattices [23,24], which demonstrated that strength and stiffness can be increased by an order of magnitude by tuning nanolattice geometry while maintaining a constant relative density [24]. Metallic glass nanolattices have been studied less frequently than metal or ceramic nanolattices due to experimental difficulties in extending the fabrication process to metallic glass.

Some studies have attempted to impart plasticity to metallic glasses by utilizing stochastic architectures, or metallic glass foams with a random distribution of heterogeneities and pores. Stochastic metallic glass foams have been fabricated by incorporating gas into metallic glass during processing [25,26] or by creating a two-phase mixture of metallic glass and another material, which is subsequently removed [27-29]. One study found ~80% compressive ductility for open-cell Zr-based amorphous metal foams with relative densities of 14-28% and pores sizes of 150-355 μm [30] Another study found that the commercial glass-forming alloy Vit106, which exhibits no significant plasticity in the monolithic alloy, can become ductile under compression, reaching ~50% strain, when it is made into an open-cell foam with porosity ~78% and pore size 212-250 μm [31]. In another study, open-cell $Zr_{41.25}Ti_{13.75}Cu_{12.5}Ni_{10}Be_{22.5}$ metallic glass foams, fabricated by using NaCl as a space-holder material, were shown to exhibit high energy absorption capacity with ductile cracking resulting from the complex stress state that arises from the presence of pores in the foam [32]. These and other stochastic cellular structures almost always contain imperfections, which render them difficult to manipulate and study

systematically. The randomness in their mesoscale architecture also naturally leads to a reduction in mechanical performance, i.e. stiffness and strength, compared with periodically ordered metallic glass foams [33-35].

Periodically architected foams may be precisely engineered to attain optimal mechanical performance. Studies on such periodically architected metallic glass foams have been limited due to the difficulty in fabricating such materials, particularly in 3D. One study utilized thermoplastic replication of metallic glass to fabricate 2D metallic glass cellular structures that ranged from perfectly periodic to highly stochastic [35]. These authors observed that while the periodic structures generally had a higher elastic modulus and yield strength compared to stochastic structures, the stochastic onees exhibited higher flaw tolerance [35]. To create 3D periodically architected metallic glass structures, one study utilized thermoplastic forming-based patterning of metallic glass sheets combined with parallel joining, which resulted in honeycomb-like architectures exhibiting high elastic energy storability and absorption [36]. 3D periodically architected metallic glass cellular structures were also fabricated using electroless deposition of Ni-P metallic glass onto a sacrificial polymer microlattice [37]. These Ni-P microlattices consisted of ~1 mm unit cells with metallic glass wall thicknesses of 60 – 600 nm and reported structures with wall thicknesses above 150 nm failed catastrophically while those with wall thicknesses below 150 nm failed with plasticity [37]. The dimensions of metallic glass lattices in nearly all of these existing studies were far from the nanoscale, including ~1 mm unit cells and 20-70 μm wall thicknesses [35], cm-sized unit cells and ~0.4 mm wall thickness [36]. and mm-sized unit cells and ~60-600 nm wall thicknesses [37]. In designing periodically nano-architected metallic glasses, both the periodic and nanoscale aspects are key to take advantage of both structural and material size effects. Experimental difficulty in fabricating hollow metallic glass nanolattices has resulted in a dearth of studies on that length scale. The only study to date

on metallic glass nanolattices [38] did not consider several factors in nanolattice fabrication and characterization, which will be discussed in section 4.3. That study did report a promising suppression of brittle failure as the $Cu_{60}Zr_{40}$ metallic glass tube-wall thickness was decreased [38].

We report the fabrication of hollow Zr-Ni-Al metallic glass nanolattices with median beam wall thicknesses of 10, 20, 30, 38, 57, and 88 nm fabricated by sputter deposition for the durations of 15, 30, 45, 60, 120, and 240 minutes, respectively. In-situ nanomechanical experiments demonstrate that reducing the wall thickness leads to a transition in the deformation behavior of the metallic glass nanolattices from catastrophic failure with large strain bursts in thick-walled nanolattices (wall thicknesses greater than ~50 nm) to smooth continuous deformation with gradual layer-by-layer collapse in thinner-walled nanolattices.

2. Experimental Section

2.1. Fabrication of hollow metallic glass nanolattices

Hollow metallic glass nanolattices were fabricated through the multi-step process shown schematically in **Figure A1** of the Appendix A. The basic steps in this nanolattice fabrication process were originally established for other material systems [18-20,23]. First, polymer scaffolds were fabricated utilizing the direct-laser-writing two-photon lithography process developed by Nanoscribe GmbH. The 3D geometry of the polymer scaffold was chosen as repeating ~7 μm octahedron unit cells connected at their vertices, as shown in **Figure 1 (a)**. Octahedron unit cells were selected as they represent a fundamental, commonly studied geometry [19,21,23,24] and thus serve as a good base unit cell for one of the first studies on metallic glass nanolattices. Further, the lack of additional beams in an octahedron, as opposed to

octet [39] geometry, allows the unit cells to be more open, which facilitates better conformality in the sputter-deposited metallic glass coating. The ~7 μm size was chosen to maximize unit cell size to further facilitate openness of the unit cells for sputter deposition while not utilizing overly long beams, which were found to become wavy and unstable when written with the Nanoscribe. Ideally, the overall nanolattice dimensions would be maximized in order to limit edge effects and make the nanolattice more representative of larger materials with this same repeating unit cell structure. Experimental practicalities, including writing time of the polymer scaffolds with Nanoscribe, hydrogen plasma penetration into the nanolattices during etching, and the maximum load achievable in the nanomechanical testing system, limited the size of the nanolattices. Considering these experimental practicalities, each nanolattice was designed to be 5 unit cells wide by 5 unit cells long by 5.5 unit cells tall, for total dimensions of ~32 μm long, ~32 μm wide, and ~36 μm tall.

This geometry was imported into NanoWrite, the program that interfaces with the Nanoscribe two-photon lithography instrument. In the two-photon lithography process, IP-Dip photoresist was exposed to a 780-nm femtosecond pulsed laser, which was focused to a small volume (i.e. a voxel, or volume resolution element) containing sufficient energy to initiate cross-linking of the photoresist through two-photo absorption. This voxel was traced in three dimensions according to the nanolattice geometry imported into NanoWrite to create the polymer scaffold. Due to the elliptical nature of the voxel, writing circular beams required tracing the elliptical voxel in a circular motion to result in beams composed of an approximately circular cross-section with diameter ~800 nm. Following lithography, the samples were developed by 30-minute immersion in propylene glycol methyl ether acetate, cleaned in isopropyl alcohol, and then dried in a critical point dryer.

Amorphous Zr-Ni-Al was sputtered to coat these polymer scaffolds under the same conditions utilized in our previous study [11], namely by sputtering an alloyed $Zr_{56}Ni_{22}Al_{22}$ target (ACI Alloys, Inc.) with a base pressure less than 1×10^{-6} Torr using a DC power supply at 100 W with resultant voltage of 320-390 V, under 3 mTorr argon in a magnetron sputter deposition system (ATC Orion sputtering system, AJA International, Inc.). The sputter deposition time was varied at times of 15, 30, 45, 60, 120, and 240 minutes in order to vary the thickness of the metallic glass coatings on the polymer scaffolds.

After sputtering, focused-ion beam (FIB) milling was used to expose the internal polymer scaffold so that it could be subsequently etched away by hydrogen plasma. For this step, the FIB was operated at 30 keV and 1-3 nA in order to remove the metallic glass coating on two opposite faces of each nanolattice, exposing the internal polymer scaffold. The samples were then placed in a hydrogen plasma system (Zepto Plasma System, Diener) operating at 100 W and 0.7 mbar to etch away the internal polymer scaffold, resulting in hollow beam nanolattices with beam walls consisting of nanoscale thicknesses of the sputtered metallic glass. The hydrogen plasma etching process took several weeks to completely remove the internal polymer scaffold. Due to the long nature of this process, the nanolattices were periodically removed from the plasma machine and imaged via SEM to monitor the etching progress. Changes in contrast as the polymer was etched were readily apparent from SEM images; a visible front of contrast change proceeded from the FIBed edges towards the center of the nanolattice as the polymer etching front advanced, as shown in **Figure A2** of the Appendix A. The nanolattices were kept in hydrogen plasma until all visible traces of polymer were removed.

2.2.   **Wall thickness analysis**

To assess the variation in wall thickness resulting from the anisotropic sputter deposition process, FIB was used to remove regions of the nanolattices and expose various cross-sections of the nanolattices from which the wall thickness of each side of each exposed beam could be measured via SEM. One such resultant cross-section was shown in **Figure 1** with higher magnification images from each unit cell arranged from top to bottom, illustrating the variation in wall thickness that results from top to bottom in the nanolattices. These cross-sectional cuts and the corresponding measurements were performed at six different locations in each measured nanolattice, ranging from the outermost side to the most interior unit cells in order to assess the variation in wall thickness that occurs from outside to inside. From each cross-sectional cut, ~20 measurements of wall thickness were performed on beams favorably oriented with the ~52° tilt of the SEM stage utilized for FIB operation. With these six cross-sectional cuts and 20 measurements for each cut, there was a representative sample of ~120 wall thickness measurements spanning the entire nanolattice from which the median and average wall thickness were determined. This measurement procedure was conducted on nanolattices fabricated with the longer sputter deposition times of 60, 120, and 240 minutes. For the shorter sputter deposition times of 15, 30, and 45 minutes, it was difficult to measure the wall thickness accurately by SEM; therefore, the wall thickness was estimated by assuming a linear variation between 0 and the wall thickness resulting from the 60-minute sputter deposition.

2.3.   Microstructural analysis

The TEM sample picture in **Figure 2** was prepared from a nanolattice fabricated by sputter deposition for the shortest time of 15 minutes, with wall thickness ~10 nm, after all the fabrication steps shown in the Appendix **Figure A1**. The nanolattice was transferred to the post

of a TEM grid (PELCO, FIB lift out TEM grid) using a micromanipulator, secured with silver conductive epoxy (H2OE EPO-TEK, Ted Pella, Inc.) allowed to cure at room temperature, and thinned with FIB. TEM was performed using a 200 keV TEM (TF20, FEI Co.).

2.4. Uniaxial compression experiments

In-situ uniaxial compression experiments on individual nanolattices were performed quasi-statically at a constant nominal strain rate of 1×10^{-3} s^{-1} in the InSEM, a combined SEM (Quanta SEM, FEI Co.) and nanoindenter (Nanomechanics, Inc.). The nanoindenter was fitted with a boron-doped diamond 170-µm flat punch. After accounting for response from the load frame and support spring, the raw load and displacement due to deformation of the nanolattice were recorded at a data acquisition rate of 100 Hz. Using this load (P) and displacement (Δl) data, engineering stress and strain were calculated using the initial nanolattice height (l_0) and footprint area (A_0) according to $\sigma_E = P/A_0$ and $\varepsilon_E = \Delta l/l_0$, where σ_E is the engineering stress and ε_E engineering strain. The initial nanolattice height and footprint area were measured by SEM images of each nanolattice prior to testing. Elastic modulus was calculated from the slope of the loading curve, using stress-strain data from the initial linear region after any initial loading instabilities. The yield strength was determined by offsetting the linear fit of the elastic modulus by 0.02% strain and finding the intersection of that offset line with the stress-strain data. The average elastic modulus and average yield strength for each nanolattice wall thickness were calculated from a minimum of 20 sets of compression data. The size of the first strain burst was measured for each data set using MATLAB to find the range of strain around the first strain burst over which the stress was continually decreasing.

Conducting compression experiments with the InSEM system allowed simultaneous compression and visualization, which facilitated a deeper understanding of the deformation behavior of individual nanolattices. The compression experiments were conducted under identical SEM imaging conditions, namely 2 keV, spot size 3, and a magnification of 6000x. There was no discernible difference in the mechanical behavior of the nanolattices observed when the electron beam was off, thus any effects of the electron beam can be considered negligible.

3. Results

3.1. Characterization of nanolattices

We designed the metallic glass nanolattices to consist of repeating ~7 μm octahedron unit cells connected at their vertices, with each nanolattice being 5 unit cells long, 5 unit cells wide, and 5.5 unit cells tall. The basic steps in the fabrication process were first developed for other materials systems, as discussed elsewhere [18-20,23]. The main departure in this work is the use of hydrogen (as opposed to oxygen) plasma to remove the polymer scaffold after the deposition of metallic glass coating to avoid oxidation of the metallic glass. More details of the fabrication steps utilized in the current study are provided in section 2.1. **Figure 1 (a)** shows an SEM image of a typical hollow Zr-Ni-Al metallic glass nanolattice.

We found the wall thickness of the beams within a single nanolattice to vary substantially, presumably due to the directional nature of sputter deposition. The sputtering process involves the bombardment of argon ions onto a $Zr_{56}Ni_{22}Al_{22}$ sputtering target, which causes the target atoms to be ejected and deposited onto the nanolattices in a manner that favors line-of-sight

deposition. This directional sputtering process results in a metallic glass coating on the nanolattices that is non-conformal, with larger wall thicknesses on the top surfaces and outer unit cells of the nanolattices. **Figure 1 (e-i)** are SEM images of cross-sections exposed at different heights within a single nanolattice fabricated for the longest sputter deposition time of 240 minutes, which resulted in the largest wall thickness variation within individual nanolattices. **Figure 1 (c)** is a top-down image of that nanolattice with the gray rectangle denoting the region of the nanolattice that was removed by FIB and the white dotted line denoting the exposed cross-section, which is shown in **Figure 1 (d)**. Higher magnification images of each unit cell in this cross-section are shown in **Figure 1 (e-i)** and are ordered from the top unit cell closest to sputter target to the bottom-most unit cell closest to the substrate. There is a visible decrease in wall thickness of the nanolattice beams as rastered from the top to bottom unit cells. What is particularly clear from these images is that the top surfaces of the topmost beams are significantly thicker compared to the lower beams. The top surfaces are expected to have thicker walls because these surfaces were directly in line-of-sight of the sputtered target atoms. The 240-minute sputter deposition, which resulted in an 88 nm median wall thickness and 114 nm average wall thickness, resulted in wall thicknesses on the top surfaces of the top beams around ~900 nm, which is similar to observed film thickness of ~1 μm on the surrounding flat substrate. For the sputter deposition time of 240 minutes, there is an order of magnitude difference between the median wall thickness of the nanolattice beams (~88 nm) and the thickness of a thin film deposited on a flat substrate (~1 μm). This demonstrates the potentially large error introduced by assuming the sputter deposition rate onto a complex 3D geometry is equal to the sputter deposition rate onto a completely flat substrate, which was the assumption used in the only previous study on metallic glass nanolattices to date [38].

It should be noted that the sputtering conditions in the current work were not fully optimized for deposition conformality as experimental limitations prevented full exploration of sputtering parameter space. With detailed analysis of sputtering conditions, it is likely that a more conformal coating could be achieved. Some parameters of interest include: target-to-sample distance and angle, rotational speed of sample stage, gas pressure, energy, and utilizing a combinatorial sputtering method. Such study would be an excellent next step in developing sputtering as a more robust technique for fabricating nano-architected metallic glasses.

In the current work, the time of sputter deposition was varied to produce nanolattices with a range of wall thicknesses. The wall thicknesses were measured by the cross-sectional analysis procedure discussed in section 2.2 and illustrated in **Figure 1 (c-i)**. The table shown in **Figure 1 (b)** notes the median and average wall thicknesses resulting from sputter deposition times of 60, 120, and 240 minutes. Sputter deposition times of 15, 30, and 45 minutes resulted in walls too thin to reliably measure via SEM, hence the wall thicknesses for those times are estimated. The average wall thickness is skewed by the large values measured from the top surfaces of the nanolattices, which do not undergo significant deformation during compression. We use the median wall thickness, which is more representative of the wall thickness for the beams undergoing deformation, to refer to each set of data. It should be emphasized that the median wall thickness is a reference point utilized mostly as a matter of convenience in referring to the data. In reality, each sputter deposition time results in a distribution of wall thicknesses throughout an individual nanolattice, with that distribution shifting to larger wall thicknesses with increased sputter deposition time. Appendix A **Figure A3** shows the measured wall thickness distributions for sputter deposition times of 240, 120, and 60 minutes, which correspond to median wall thicknesses of 88, 57, and 38 nm, respectively. These wall thickness

distributions exhibit significant overlap but do shift to larger wall thicknesses with increased sputter deposition time.

Figure 2 displays transmission electron microscope (TEM) images of a nanolattice section with a ~10 nm wall thickness (sputter deposition time of 15 minutes) after all the fabrication steps. Details of the TEM sample preparation are provided in section 2.3. Figure 2 (a) shows a low-magnification TEM image of an entire unit cell of the nanolattice. The FIB thinning utilized to prepare the nanolattice for TEM resulted in some changes to the shape of the beams and arrangement of unit cells in the nanolattice structure. Figure 2 (b) contains the diffraction pattern obtained from the region of the nanolattice marked with a star in Figure 2 (a). The diffuse rings in the diffraction pattern confirm the amorphous structure of the nanolattice after all fabrication steps, which is corroborated by the lack of ordering observed in the high resolution TEM image (Figure 2 (c)). We examined other regions in the nanolattice via TEM and found consistent characteristic amorphous diffraction patterns and images with no evidence of nanocrystallites. Energy-dispersive x-ray spectroscopy (EDS) revealed the stoichiometry of the deposited metallic glass to be $Zr_{54}Ni_{28}Al_{18}$.

3.2.   Compression experiments on nanolattices of various wall thicknesses

Figure 3 (a) contains representative engineering stress-strain data obtained via uniaxial compression to ~67% strain on nanolattices with wall thicknesses ranging from ~10 nm to ~88 nm. The nanolattices with thicker walls (~57 nm and ~88 nm) were difficult to compress to exactly 67% strain because of the frequent strain busts associated with their deformation, which correspond to failure of the nanolattice layers. One such strain burst is shown in Figure 3 (a) between points I and II. The mechanical response of thinner-walled nanolattices becomes more

deformable, as demonstrated by the shorter strain bursts and smoother, more continuous stress-strain data, as can be observed in **Figure 3 (a)** points I′-IV′. The in-situ images shown in **Figure 3 (I-IV)** visualize the deformation of a typical nanolattice with ~88 nm wall thickness nanolattice, which exhibits catastrophic destruction of nanolattice layers with large strain bursts. **Figure 3 (I′-IV′)** shows a similar sequence of images for a nanolattice with ~20 nm wall thickness, which exhibits gradual layer-by-layer collapse and folding up of nanolattice layers on top of each other.

These differences in mechanical response are also depicted in **Figure 4**, which displays all the stress-strain data grouped by wall thickness under compression to various strains. **Figure 4** is particularly helpful for visualizing details of the stress-strain response for thinner-walled nanolattices, which are at the low end of the engineering stress scale used in **Figure 3 (a)**. A minimum of 14 nanolattices were compressed for each wall thickness and the breadth of the data displayed in **Figure 4** for each wall thickness demonstrates the consistency and repeatability of these compression experiments.

The stress-strain data of the thinnest-walled nanolattices, ones with wall thicknesses of ~10 nm (**Figure 4 (a)**) and ~20 nm (**Figure 4 (b)**), is characterized by smooth, continuous deformation (see **Video 1** for the ~10 nm wall thickness and **Video 2** for the ~20 nm wall thickness). The presence of three undulations in the stress-strain data over strains of 0 to 0.4 correspond to a gradual layer-by-layer collapse. Each undulation corresponds to the failure of an individual layer, which carries load until reaching a peak stress and then gradually, folds up and collapses, which drives the stress decreases. **Figure 5** shows the image of a typical post-compression nanolattice with a wall thickness of ~10 nm, which underwent such a layer-by-layer collapse. The layers neatly folded up underneath one another with no catastrophic damage to the

nanolattice and with the beams remaining intact and the general structure of the unit cells still apparent. The failure of individual layers in this mechanism always involves collapse of the beams in the bottom half of each unit cell first while those in the top-half of each unit cell are largely unchanged during compression. This likely occurs due to variation in wall thickness that results from the directional nature of sputter deposition, leading to thicker-walled beams in the top half of each unit cell. The thinner bottom beams of each unit cell more readily deform than their thicker counterparts, hence most failure of individual layers is localized to the bottom beams, as visualized in **Figure 5**.

As the wall thickness of the nanolattice beams increases, the stress-strain response becomes more discontinuous, as shown in the stress-strain data for the nanolattices with a wall thickness of ~30 nm (**Figure 4 (c)**) and those with a wall thickness of ~38 nm (**Figure 4 (d)**). See also **Video 3** for the ~30 nm wall thickness and **Video 4** for the ~38 nm wall thickness. These nanolattices with intermediate wall thicknesses exhibit some characteristics of the layer-by-layer collapse observed in the thinnest-walled nanolattices (**Figure 4 (a, b)**); with less pronounced undulations and the addition of small strain bursts to the data. The strain bursts are caused by rapid failure events, such as a beam breaking or a layer of unit cells failing. These rapid failure events often happen too quickly for the nanoindenter to capture data at the 100 Hz data acquisition rate, resulting in the observed discontinuities in the stress-strain data. The largest strain burst in these intermediate wall thickness nanolattices almost always occurred immediately after elastic loading and usually involved partial catastrophic failure of a nanolattice layer, unlike the gradual collapse of nanolattice layers observed for the thinnest walled nanolattices. After this incipient failure event, the deformation commenced via smaller strain bursts, similar to serrated flow in metallic glasses, with each serration representing a relaxation event associated with the

formation and propagation of a shear band. After a single shear band activates and terminates, the nanolattice can be deformed further through successive shear banding events upon subsequent loading.

The thickest-walled nanolattices, ones with wall thicknesses of ~57 nm (**Figure 4 (e)**) and ~88 nm (**Figure 4 (f)**), deform by sudden failure events and large catastrophic strain bursts that are characteristic of brittle failure (see **Video 5** for the ~57 nm wall thickness and **Video 6** for the ~88 nm wall thickness). The catastrophic nature of the failure in these thick-walled nanolattices is also illustrated in **Figure 6**, which depicts a nanolattice with a wall thickness ~88 nm after compression to 33% strain and unloading. The two layers in the middle of the nanolattice have catastrophically failed with the original structure of those unit cells destroyed and no longer intact.

3.2.1. Analysis of First Strain Burst

The experiments reveal that the wall thickness largely dictates the nature of post-elastic deformation. Following elastic loading, some nanolattices undergo gradual deformation, while others exhibit a sudden failure event or strain burst. The nature of this first strain burst is determined by the wall thickness. The thinnest-walled nanolattices, **Figure 4 (a, b)**, exhibit gradual deformation with no strain burst after elastic loading, the nanolattices with intermediate wall thicknesses, (**Figure 4 (c, d)**), exhibit a small strain burst following elastic loading, and the thickest-walled nanolattices, **Figure 4 (e, f)**, exhibit a very large strain burst after elastic loading. **Figure 7** depicts these dramatic changes in the first strain burst for nanolattices of different wall thicknesses. **Figure 7 (a-h)** contains representative SEM images of the nanolattices that exhibit a first strain burst immediately before and after the strain burst occurs. These images illustrate the regions within the nanolattices that fail as a consequence of the first strain burst. Each nanolattice

contains 5.5 layers of unit cells and the first strain burst usually initializes in the fourth layer of unit cells from the top. The nanolattices with ~30 nm wall thickness fail in the fourth layer of unit cells with only a partial collapse of that layer, the ~38 nm wall thickness nanolattices also fail in the fourth layer of unit cells with a larger partial collapse of that layer, the ~57 nm wall thickness nanolattices fail with complete destruction of the entire fourth layer of unit cells, and the ~88 nm wall thickness nanolattices fail with complete destruction of the entire third and fourth layers of unit cells. Failure usually initiates at the fourth layer of unit cells likely because the anisotropic sputter deposition results in this layer of unit cells having the thinnest walls. The wall thickness of sputter-deposited nanolattice beams generally decreases from top to bottom in the nanolattice, although the bottommost layers are thicker because of the redeposition of atoms from the thin film growing on the substrate surface during sputtering. The fourth layer of unit cells, which is towards the bottom of the nanolattice but not so far down as to have redeposition from the thin film on the substrate, has the thinnest walls, thereby deforming most easily.

The stress-strain data corresponding to the SEM images of **Figure 7 (a-h)** are included immediately below the SEM images for more quantitative assessment of the stress and strain changes during the first strain burst. **Figure 7 (i)** displays the average size of the first strain burst as a function of the beam wall thickness. We obtained the average strain burst size for each wall thickness from a minimum of 16 sets of stress-strain data of individual nanolattices. As the thinnest-walled nanolattices (~10 nm and ~20 nm wall thicknesses) deformed gradually, with no strain bursts, the size of the strain burst for these samples is shown as 0. For the wall thicknesses of ~30 nm and greater, the size of the strain burst increases linearly with wall thickness.

The absolute size of the first strain burst in these types of experiments depends on the details of the compression test method and controls and on the dynamics of the mechanical testing

instrument. All nanolattices in this work were compressed using an identical test method and mechanical testing instrument, which allows for a comparison of strain burst size. The sizes of these strain bursts may vary with other mechanical testing instruments and test methods; hence, care should be taken in comparing strain burst size in this study with that in another study using disparate testing conditions and instrumentation. Details of the mechanical experiments and instrumentation are provided in section 2.4.

3.2.2. Nanolattice Recovery

Another way to assess post-elastic deformation is by considering nanolattice recovery following compression and unloading. **Figure 8** shows the differences in recovery between the thinnest-walled nanolattices (**Figure 8 (a, b)**) and the thickest-walled nanolattices (**Figure 8 (c, d)**) after compression to 33% strain. The thinner-walled nanolattices recover more readily than thicker-walled nanolattices, which exhibited catastrophic failure and destruction of the unit cell structure making up the failed layers. Recovery was measured from nanolattices compressed to 33% strain because the first strain burst in nanolattices with the thickest walls resulted in compression to a minimum strain of ~33% as 2 of the 5.5 layers of unit cells failed simultaneously. In addition, it was desirable to measure recovery from a strain that underwent significant plasticity, yet not too much strain that the original nanolattice structure was completely destroyed. Recovery was defined as,

$$recovery = \frac{\Delta l_{recovered}}{\Delta l_{compressed}} \tag{1}$$

where $\Delta l_{compressed}$ is the total compressive displacement, $\Delta l_{recovered}$ is the height of nanolattice immediately after unloading ($h_{after\ unloading}$) less the height of the nanolattice under the maximum compressive strain ($h_{max\ compression}$),

$$\Delta l_{recovered} = h_{after\ unloading} - h_{max\ compression} \qquad (2)$$

These recovery measurements are shown in **Figure 8 (e)** with the emergence of a general trend that recovery decreases linearly with wall thickness. We chose to focus on recovery after compression to 33% strain, which limited this analysis to contain only a single data point for each wall thickness.

3.2.3. Elastic Modulus and Yield Strength of the Nanolattices

The elastic modulus (E) and yield strength (σ_y) were measured by considering the stress-strain response of the nanolattices at low strains. The same stress-strain data plotted in **Figure 4** is plotted in **Figure 9 (a-f)** over the low strain region of 0 to 0.05 to illustrate the region of interest for determination of elastic modulus and yield strength. The data is grouped by nanolattice wall thickness, with each plot containing a dotted horizontal line that denotes the average measured yield strength and a dashed line with a slope that dentoes the average measured elastic modulus for the particular wall thickness of the plot. The procedure used for determination of E and σ_y is provided in section 2.4. The average elastic modulus and yield strength for each nanolattice wall thickness are plotted as a function of nanolattice relative density in Appendix A **Figure A4**. Relative density is defined as the volume fraction of the solid material in the nanolattice [40]. We estimated nanolattice relative density using SolidWorks models of the nanolattice geometry with a uniform wall thickness, assumed to be the median measured wall thickness for each sputter deposition time (**Figure 1 (b)**).

The large variation in the nanolattice wall thickness renders an accurate determination of a single relative density for each nanolattice unreliable. The relative density is expected to be lower in the regions of the nanolattice with thinner walls, such as the interior and lower regions of the nanolattice, and higher in the regions of the nanolattice with thicker walls, such as the top and outer sides. There are also local variations in wall thickness within a single unit cell (top beams have thicker walls than bottom beams) and within a single beam (the top surfaces of beams have thicker walls than bottom surfaces). All of these factors suggest that the relative densities plotted in **Figure S2** should be taken only as estimates.

Plots of elastic modulus and yield strength as a function of relative density are frequently utilized as figures of merit in evaluating and comparing the mechanical properties of cellular solids. The strength (σ) and elastic modulus (E) of a cellular solid are related to its relative density ($\bar{\rho}$) as $E \propto \bar{\rho}^m$ and $\sigma \propto \bar{\rho}^n$, where the exponents m and n depend solely on the fundamental deformation mechanism of the cellular solid architecture, involving either bending or stretching of the beams upon loading [40-42]. The octahedron unit cells of the current work are bending-dominated and would be expected to have a scaling with relative density that follows the relations, $E \propto \bar{\rho}^2$ and $\sigma \propto \bar{\rho}^{1.5}$ [39-41,43]. **Figure S2** shows the observed scaling of the metallic glass nanolattices in this study as $E \propto \bar{\rho}^{1.68}$ and $\sigma \propto \bar{\rho}^{1.74}$, which deviate significantly from the theoretical predicted values. As discussed previously, the relative densities of the nanolattices were calculated with the assumption of a constant beam wall thickness equal to the measured median wall thickness, which renders the relative densities and thus the resultant scaling exponents inaccurate. Not many conclusions can be drawn from the scaling behavior of nanolattices fabricated by sputtering or other techniques that lead to large variations in wall thickness, and hence in in relative density throughout individual nanolattices.

It is also instructive to plot the elastic modulus and yield strength as a function of density in what are commonly known as material property charts, or Ashby plots, which are helpful in materials selection [1,43]. **Figure 9 (g-h)** shows the elastic modulus and yield strength of the metallic glass nanolattices from this work plotted versus density and overlaid on the property space of existing materials. The metallic glass nanolattices fall in the same material property space as foams and span a large range of densities. For comparison, the elastic modulus and yield strength of bulk sputtered $Zr_{54}Ni_{28}Al_{18}$ metallic glass are also plotted and are marked with stars. The average bulk yield strength of 1.26 GPa was determined from the nano-tensile experiments in our previous study [11]. The elastic modulus of this as-sputtered metallic glass was determined to be 130 GPa, measaured by nanoindentation into a ~1 µm-thick film using the Oliver-Pharr method [44]. The density used for the plots in **Figure 9 (g-h)** was calculated by multiplying the assumed bulk density of $Zr_{54}Ni_{28}Al_{18}$ (6481.7 kg m^{-3}) by relative density of the nanolattice, determined by SolidWorks models as described above. The anisotropic nature of sputter deposition leads to variation in wall thickness throughout each nanolattice which makes accurate determination of relative density difficult, as discussed above. As such, the densities plotted for the metallic glass nanolattices in **Figure 9 (g-h)** should be taken only as estimates useful for showing the approximate location of the metallic glass nanolattices in material property space relative to other materials.

4. Discussion

The nanolattices in this study exhibit a mechanical response that is a result of a combination of structural effects from the lattice geometry and material size effects from the nano-sized constituent metallic glass. To gain a complete understanding of why the observed brittle-to-

deformable transition occurs as wall thickness is reduced, it is important to evaluate how much each of these effects contributes to the mechanical response of the nanolattices.

4.1. Nanolattice structural effects

Arranging the metallic glass into a periodic structure of octahedron unit cells necessitates consideration of potential failure mechanisms resulting from the structure. The work of Meza et. al [20] predicts that failure of a nanolattice will occur via one of three potential mechanisms: material yielding, local shell buckling, or Euler beam buckling. These failure mechanisms can be defined as [45]:

$$\sigma_{yield} = \sigma_y \tag{3}$$

$$\sigma_{shell} = \frac{E}{\sqrt{3(1 - \nu^2)}}\left(\frac{t}{r}\right) \tag{4}$$

$$\sigma_{beam} = \frac{\pi^2 EI}{(kL)^2 A_{beam}} \tag{5}$$

where σ_y, E, and ν are the yield strength, elastic modulus, and Poisson's ratio of the constituent metallic glass, respectively. k is a constant based on the boundary conditions of the beams, which can be taken as ~0.6 for the octahedron geometry [46]. L is the beam length, t is the beam's wall thickness, A_{beam} is the cross-sectional area of the beam, and I is the area moment of inertia for the beam. For the thin-walled, approximately circular-cross-section beams that comprise the nanolattices in this work, these parameters are given by

$$A_{beam} = 2\pi rt \tag{6}$$

$$I = \pi r^3 t \tag{7}$$

Substituting Equations 6 and 7 into Equation 5, we find that the Euler buckling failure criterion is given by

$$\sigma_{beam} = \frac{25}{18}\pi^2 E \left(\frac{r}{L}\right)^2 \qquad (8)$$

As discussed by Meza et. al [20], two failure mechanisms exist for nanolattices: yielding versus local shell buckling and yielding versus Euler beam buckling. These failure mechanisms may act in combination or independently. Yielding will occur under tension and buckling will occur under compression [20]. The complex stress-state in the hollow beam nanolattices leads to certain beams and regions being under compression while other beam and regions are under tension [20]. For example, in the octahedron unit cells making up the nanolattices of this work, the four horizontal beams are largely under tension while the eight vertical beams are largely under compression. Further, the bending of hollow beams near the nodes leads to stress concentrations at the nodes. The nodes often serve as the location within the nanolattice where failure first initiates, regardless of the nature of deformation. For example, failure initiates by gradual node bending for thin-walled nanolattices (Figure 5) and by fracture-like behavior at the nodes for thick-walled nanolattices (Figure 6).

Assuming the compressive and tensile stresses in the nanolattice are roughly equal, which is reasonable for beams in bending [20], the critical transition criteria between the failure mechanisms can be found by setting the failure equations equal to each other, such that Equation 3 is set equal to Equation 4, to find the transition between yielding and local shell buckling,

$$\sigma_{yield} = \sigma_{shell} \longrightarrow \left(\frac{t}{r}\right)_{crit} = \frac{\sigma_y}{E}\sqrt{3(1-\nu^2)} \qquad (9)$$

Similarly, Equation 3 is set equal to Equation 8 to find the transition between yielding and Euler beam buckling,

$$\sigma_{yield} = \sigma_{beam} \rightarrow \left(\frac{r}{L}\right)_{crit} = \frac{3}{5\pi}\sqrt{\frac{2\sigma_y}{E}} \tag{10}$$

Equation 9 and 10 are functions of only the constituent properties for the bulk Zr-Ni-Al metallic glass that makes up the nanolattices and not of any structural parameters. As in the material property charts of **Figure 9 (g, h)**, the bulk properties for yield strength and elastic modulus of the sputtered Zr-Ni-Al metallic glass were taken as 1.26 GPa and 130 GPa respectively. We assumed the Poisson's ratio for the metallic glass to be 0.36 as the Poisson's ratio for Zr-based metallic glasses have been reported to range from 0.35-0.37 [47]. Substituting these values into equations 9 and 10, we find the critical local shell buckling transition to occur at $(t/r)_{crit} = 0.016$ and the critical Euler beam buckling transition is found to occur at $(r/L)_{crit} = 0.027$. Considering only these structural effects, nanolattices with values of wall thickness (t), beam radius (r), and beam length (L) such that (t/r) and (r/L) are greater than these critical ratios would be expected to fail by yielding with no structural buckling.

In this work, the nanolattices with the thinnest walls (median wall thickness ~10 nm) would be most susceptible to local (shell) buckling. These thinnest-walled nanolattices have (t/r)=(10 nm/400 nm)=0.025, which is greater than the critical value for shell-buckling of $(t/r)_{crit} = 0.016$, therefore the nanolattices in this work would not be expected to exhibit local (shell) buckling. However, there are locations within the nanolattice where the wall thickness is thinner than the median thickness, thus there may be local regions that meet the criterion for shell buckling. Considering Euler beam buckling, the nanolattices in this study contain (r/L) = (0.4 μm/4.9 μm) = 0.081, which is greater than the critical value for Euler beam buckling of $(r/L)_{crit} = 0.027$, and thus the nanolattices in this study would also not be expected to exhibit Euler beam buckling. These calculations reveal that the structure of the nanolattices in this work is such that local shell

26

buckling and Euler beam buckling are likely suppressed, and the primary failure mechanism is yielding. As a result, the metallic glass material of the nanolattice, as opposed to the structure of the nanolattice, determines the dominant failure behavior.

4.2.   Material size effects in metallic glasses

The structural analysis in the previous section demonstrates that the geometry of the structure is not within the range where Euler beam buckling or local (shell) buckling is expected to occur. This indicates the observed changes in deformation behavior from brittle catastrophic failure in thick-walled nanolattices to deformable ductile-like behavior in thin-walled nanolattices are caused by the metallic glass. The observed brittle-to-ductile transition that oc*curs as the wall thickness of nanolattice beams decreases is analogous to the brittle-to-ductile transition that has been frequently observed as the sample diameter is reduced in metallic glass nanopillars [5-11].*

The "smaller is more ductile or deformable" size effect frequently observed in metallic glass nanopillars has predominantly been rationalized by the high surface-to-volume ratio in nanopillar samples, which increases the energetic cost of forming and propagating a shear band compared to homogeneous deformation [6,8,9,48-50]. For a sample of dimension, L, the energy required for a crack-like shear band to propagate scales with the sample cross-sectional area, or $E_{shear\ band} \sim L^2$ while the energy required to deform a sample in a homogeneous way scales with the sample volume, or $E_{homogeneous} \sim L^3$. As the sample dimension is reduced L^3 decreases faster than L^2, which means that shear band propagation may become energetically unfavorable in nanoscale volumes. Analogous to Griffith criterion for crack propagation, these energetic scaling arguments can be further used to estimate the critical stress for shear band formation [6,8].

The size effect has also been rationalized by considering that small samples may be smaller than certain deformation units within metallic glasses, such as shear transformation zones or the plastic zone size [12]. Some studies reported that for a shear band to be fully developed and propagate, its nucleus would need to be at least ~50-500 nm [4,9,51], which means that small nanoscale samples may not provide sufficient space for shear banding to occur. Another deformation unit relevant at even larger length scales is the plastic zone size at the tip of an

incipient crack, which can be micron-sized or larger. If the plastic zone size is greater than the sample size then brittle failure is not expected [1] and bending plasticity is greatly enhanced when the plastic zone is larger than half the sample thickness [52-54].

4.3.   Comparison to previous work on metallic glass nanolattices

Despite the abundance of studies on the "smaller is more deformable" size effect in metallic glass nanopillars [5-11], this is one of the first studies on proliferation of such a size effect to metallic glass nanolattices. As discussed in section 1, experimental difficulty in fabricating hollow metallic glass nanolattices has resulted in few studies on the subject. The only study to date on metallic glass nanolattices [38] did not consider some aspects of nanolattice fabrication and characterization. The reported oxygen plasma etch time to remove the nanolattice polymer core was 2.5 hours [38], which is more than an order of magnitude less that previous reports of 50-75 hours [20]. Careful inspection of SEM images in that previous study [38] suggests that the polymer core was not removed. The nanolattices of that study were composed of $Cu_{60}Zr_{40}$ metallic glass [38], which visibly oxidizes (changing in color from shiny silver to charred black) when placed in oxygen plasma. It is then possible that the metallic glass nanolattices in that study may have partially oxidized and were not hollow. Further, the wall thickness of the nanolattices in that previous study [38] was assumed to be given by the deposition rate when sputtering onto a flat substrate. As demonstrated in section 3.1, the deposition rate onto nanolattices can be an order of magnitude slower than that onto a flat substrate. Sputtering onto nanolattices also results in significant variation of the wall thickness within individual nanolattices, which necessitates detailed analysis to determine the wall thickness distribution. The methodology choices in the only previous study on metallic glass nanolattices [38] to date

warrant additional study on conclusively hollow metallic glass nanolattices with more accurately measured wall thicknesses, which was the aim of the current work.

5. Conclusion

We demonstrated the fabrication of hollow metallic glass nanolattices with the constituent metallic glass deposited by sputtering. The sputter deposition was conducted for various times to result in nanolattices with different wall thicknesses, with the median wall thickness ranging from 10 nm to 88 nm. Uniaxial compression experiments performed inside of an SEM revealed a brittle-to-deformable transition as the nanolattice wall thickness is reduced. Thick-walled nanolattices exhibited large catastrophic strain bursts characterized by simultaneous failure of multiple nanolattice layers. Thin-walled nanolattices exhibited no strain bursts and instead underwent smooth continuous deformation, with gradual layer-by-layer collapse and substantial recovery upon unloading. Structural analysis indicates all nanolattices in this study are outside the regime of Euler beam buckling and local (shell) buckling, indicating the failure mode in the nanolattices of this study arise from the constituent metallic glass material, not the nanolattice structure.

The observed brittle-to-deformable transition as wall thickness is reduced can be understood in terms of the "smaller is more ductile or deformable" size effect that has been observed in existing literature on monolithic metallic glass under compression [5-7], tension [8-11], and bending [52,55]. The new insight from the current work is the demonstration that the suppression of brittle failure in nano-sized metallic glasses can indeed be proliferated to larger macroscopic structures that are subjected to complex stress states, as long as a high surface-to-volume ratio is

maintained by keeping the metallic glass nanolattice wall thickness below some critical brittle-to-ductile transition length.

5.1. Outlook and implications for nano-architected metallic glass

This work is aimed towards understanding the mechanical behavior of metallic glass nanolattices and serves as proof of concept that the "smaller is more deformable" size effect mainly observed in metallic glass nanopillars subjected to uniaxial stress states, can be extended to macroscopic materials and complex stress states through nano-architecting. This work also demonstrates that metallic glass nanolattices can be thought of as having tunable mechanical properties where parameters such as the wall thickness can be adjusted to achieve a desired mechanical response. We show the emergence of a transition in the nanolattice mechanical response under compression - from catastrophic layer failure to a deformable, gradual layer-by-layer collapse - as the wall thickness is systematically reduced. This reduction in wall thickness also comes with a significant sacrifice in strength. We found that adjusting the wall thickness of metallic glass nanolattices is not sufficient to tune the resultant mechanical response in a way the reaches the desirable material property space of simultaneous deformability and strength. Further optimization of parameters such as nanolattice geometry, constituent metallic glass, and metallic glass deposition method, with a particular focus on creating a more uniform wall thickness within each nanolattice, may result in metallic glass nanolattices with improved mechanical properties and elucidate additional knobs for tuning the mechanical response of nano-architected metallic glass.

The material property charts (**Figure 9**) illustrate that the metallic glass nanolattices fall within the existing property space for foams and do not reach new property space in the desirable

region of low density with high modulus and strength. The focus of this work was on understanding whether the "smaller is more deformable" material size effect can be proliferated to larger-scal estructures. The nanolattice geometry was not optimized for mechanical performance, and the structural analysis demonstrated that structural effects were not contributing to the enhanced deformability of the metallic glass nanolattices. Such a lack of a structural contribution to the resultant failure modes was desirable in this study to isolate and quantify the influence of the metallic glass material size effect on the mechanical response. Ordered periodic cellular solids have been shown to have higher elastic modulus and compressive yield strength compared to stochastic foams [35] and in some cases, even compared to bulk materials [56]. It is likely that with further optimization of the structure both material size effects and structural effects could combine to enhance the mechanical response of metallic glass nanolattices. Pathways to optimize the nanolattice structure include utilizing a stretching (as opposed to bending) dominated structure, which is expected to have better scaling of strength and elastic modulus with relative density, and utilizing beam geometries that favor buckling and deformability. These additional efforts promise to enable design of deformable, nano-architected metallic glasses, which would reach the untapped target region in material property space of ultralow low density with high stiffness and strength.

References

[1] M.F. Ashby, and A.L. Greer, Metallic glasses as structural materials, Scripta Materialia. 54 (2006) 321-326.

[2] M. Telford, The case for bulk metallic glass, Materials Today. 7 (2004) 36-43.

[3] H. Wang, C. Dong, and H. Shek, Bulk metallic glasses, Materials Science and Engineering R. 44 (2004) 45-89.

[4] C.A. Schuh, T.C. Hufnagel, and U. Ramamurty, Mechanical behavior of amorphous alloys, Acta Materialia. 55 (2007) 4067-4109.

[5] D. Jang, C.T. Gross, and J.R. Greer, Effects of size on the strength and deformation mechanism in Zr-based metallic glasses, International Journal of Plasticity. 27 (2011) 858-867.

[6] C.A. Volkert, A. Donohue, and F. Spaepen, Effect of sample size on deformation in amorphous metals, Journal of Applied Physics. 103 (2008) 083539-083539.

[7] O.V. Kuzmin, Y.T. Pei, C.Q. Chen, and J.T.M. De Hosson, Intrinsic and extrinsic size effects in the deformation of metallic glass nanopillars, Acta Materialia. 60 (2012) 889-898.

[8] D. Jang, and J.R. Greer, Transition from a strong-yet-brittle to a stronger-and-ductile state by size reduction of metallic glasses, Nature Materials. 9 (2010) 215-219.

[9] H. Guo, P.F. Yan, Y.B. Wang, J. Tan, Z.F. Zhang, M.L. Sui, and E. Ma, Tensile ductility and necking of metallic glass, Nature Materials. 6 (2007) 735-9.

[10] L. Tian, Z.-W. Shan, and E. Ma, Ductile necking behavior of nanoscale metallic glasses under uniaxial tension at room temperature, Acta Materialia. 61 (2013) 4823-4830.

[11] R. Liontas, M. Jafary-Zadeh, Q. Zeng, Y.-W. Zhang, W.L. Mao, and J.R. Greer, Substantial tensile ductility in sputtered Zr-Ni-Al nano-sized metallic glass, Acta Materialia. 118 (2016) 270-285.

[12] G. Kumar, A. Desai, and J. Schroers, Bulk metallic glass: the smaller the better, Adv Mater. 23 (2011) 461-76.

[13] M. Chen, A brief overview of bulk metallic glasses, NPG Asia Materials. 3 (2011) 82-90.

[14] J. Fischer, and M. Wegener, Three-dimensional optical laser lithography beyond the diffraction limit, Laser & Photonics Reviews. 7 (2013) 22-44.

[15] W. Xiong, Y.S. Zhou, X.N. He, Y. Gao, M. Mahjouri-Samani, L. Jiang, T. Baldacchini, and Y.F. Lu, Simultaneous additive and subtractive three-dimensional nanofabrication using integrated two-photon polymerization and multiphoton ablation, Light: Science & Applications. 1 (2012) e6.

[16] H.-B. Sun, and S. Kawata, Two-photon photopolymerization and 3D lithographic microfabrication, NMR 3D Analysis Photopolymerization. (2004) 169-273.

[17] L. Montemayor, V. Chernow, and J.R. Greer, Materials by design: Using architecture in material design to reach new property spaces, MRS Bulletin. 40 (2015) 1122-1129.

[18] D. Jang, L.R. Meza, F. Greer, and J.R. Greer, Fabrication and deformation of three-dimensional hollow ceramic nanostructures, Nature Materials. 12 (2013) 893-8.

[19] L.R. Meza, and J.R. Greer, Mechanical characterization of hollow ceramic nanolattices, Journal of Materials Science. 49 (2014) 2496-2508.

[20] L.R. Meza, S. Das, and J.R. Greer, Strong, lightweight, and recoverable three-dimensional ceramic nanolattices, Science. 345 (2014) 1322-6.

[21] L.R. Meza, A.J. Zelhofer, N. Clarke, A.J. Mateos, D.M. Kochmann, and J.R. Greer, Resilient 3D hierarchical architected metamaterials, Proceedings of the National Academy of Sciences of the United States of America. 112 (2015) 11502-7.

[22] L.C. Montemayor, W.H. Wong, Y.W. Zhang, and J.R. Greer, Insensitivity to Flaws Leads to Damage Tolerance in Brittle Architected Meta-Materials, Scientific Reports. 6 (2016) 20570.

[23] L.C. Montemayor, L.R. Meza, and J.R. Greer, Design and Fabrication of Hollow Rigid Nanolattices via Two-Photon Lithography, Advanced Engineering Materials. 16 (2013) 184-189.

[24] L.C. Montemayor, and J.R. Greer, Mechanical Response of Hollow Metallic Nanolattices: Combining Structural and Material Size Effects, Journal of Applied Mechanics. 82 (2015) 071012.

[25] J. Schroers, C. Veazey, and W.L. Johnson, Amorphous metallic foam, Applied Physics Letters. 82 (2003) 370-372.

[26] J. Schroers, C. Veazey, M.D. Demetriou, and W.L. Johnson, Synthesis method for amorphous metallic foam, Journal of Applied Physics. 96 (2004) 7723-7730.

[27] T. Wada, and A. Inoue, Fabrication, thermal stability and mechanical properties of porous bulk glassy Pd-Cu-Ni-P alloys, Materials Transactions. 44 (2003) 2228-2231.

[28] A.H. Brothers, R. Scheunemann, J.D. DeFouw, and D.C. Dunand, Processing and structure of open-celled amorphous metal foams, Scripta Materialia. 52 (2005) 335-339.

[29] M.H. Lee, and D.J. Sordelet, Synthesis of bulk metallic glass foam by powder extrusion with a fugitive second phase, Applied Physics Letters. 89 (2006) 21921-21921.

[30] A.H. Brothers, and D.C. Dunand, Plasticity and damage in cellular amorphous metals, Acta Materialia. 53 (2005) 4427-4440.

[31] A.H. Brothers, and D.C. Dunand, Ductile bulk metallic glass foams, Advanced Materials. 17 (2005) 484-486.

[32] X. Wei, J.H. Chen, and L.H. Dai, Energy absorption mechanism of open-cell Zr-based bulk metallic glass foam, Scripta Materialia. 66 (2012) 721-724.

[33] A.G. Evans, J.W. Hutchinson, N.A. Fleck, M.F. Ashby, and H.N.G. Wadley, The topological design of multifunctional cellular metals, Progress in Materials Science. 46 (2001) 309-327.

[34] A.G. Evans, J.W. Hutchinson, and M.F. Ashby, Multifunctionality of cellular metal systems, Progress in Materials Science. 43 (1998) 171-221.

[35] W. Chen, Z. Liu, H.M. Robinson, and J. Schroers, Flaw tolerance vs. performance: A tradeoff in metallic glass cellular structures, Acta Materialia. 73 (2014) 259-274.

[36] Z. Liu, W. Chen, J. Carstensen, J. Ketkaew, R.M.O. Mota, J.K. Guest, and J. Schroers, 3D metallic glass cellular structures, Acta Materialia. 105 (2016) 35-43.

[37] J. Rys, L. Valdevit, T.A. Schaedler, A.J. Jacobsen, W.B. Carter, and J.R. Greer, Fabrication and Deformation of Metallic Glass Micro-Lattices, Advanced Engineering Materials. 16 (2014) 889-896.

[38] S.W. Lee, M. Jafary-Zadeh, D.Z. Chen, Y.W. Zhang, and J.R. Greer, Size Effect Suppresses Brittle Failure in Hollow Cu60Zr40 Metallic Glass Nanolattices Deformed at Cryogenic Temperatures, Nano Letters. 15 (2015) 5673-81.

[39] V.S. Deshpande, N.A. Fleck, and M.F. Ashby, Effective properties of the octet-truss lattice material, Journal of the Mechanics and Physics of Solids. 49 (2001) 1747-1769.

[40] L.J. Gibson, and M.F. Ashby, Cellular solids: structure and properties, Cambridge University Press, Cambridge; New York, 1999.

[41] N.A. Fleck, V.S. Deshpande, and M.F. Ashby, Micro-architectured materials: past, present and future, Proceedings of the Royal Society of London A: Mathematical, Physical and Engineering Sciences. 466 (2010) 2495-2516.

[42] V.S. Deshpande, M.F. Ashby, and N.A. Fleck, Foam topology: bending versus stretching dominated architectures, Acta Materialia. 49 (2001) 1035-1040.

[43] M.F. Ashby, The properties of foams and lattices, Philosophical Transactions of the Royal Society A. 364 (2006) 15-30.

[44] W.C. Oliver, and G.M. Pharr, An improved technique for determining hardness and elastic modulus using load and displacement sensing indentation experiments, Journal of Materials Research. 7 (1992) 1564-1583.

[45] H.G. Allen, and P.S. Bulson, Background to Buckling, McGraw-Hill, 1980.

[46] L.R. Meza, (2016).

[47] Z. Zhang, V. Keppens, P.K. Liaw, Y. Yokoyama, and A. Inoue, Elastic properties of Zr-based bulk metallic glasses studied by resonant ultrasound spectroscopy, Journal of Materials Research. 22 (2007) 364-367.

[48] D.J. Magagnosc, R. Ehrbar, G. Kumar, M.R. He, J. Schroers, and D.S. Gianola, Tunable tensile ductility in metallic glasses, Scientific Reports. 3 (2013) 1096.

[49] D.Z. Chen, D. Jang, K.M. Guan, Q. An, W.A. Goddard, and J.R. Greer, Nanometallic glasses: size reduction brings ductility, surface state drives its extent, Nano Letters. 13 (2013) 4462-8.

[50] W.F. Wu, Z. Han, and Y. Li, Size-dependent malleable-to-brittle transition in a bulk metallic glass, Applied Physics Letters. 93 (2008) 061908.

[51] C.A. Schuh, A.C. Lund, and T.G. Nieh, New regime of homogeneous flow in the deformation map of metallic glasses: elevated temperature nanoindentation experiments and mechanistic modeling, Acta Materialia. 52 (2004) 5879-5891.

[52] R.D. Conner, W.L. Johnson, N.E. Paton, and W.D. Nix, Shear bands and cracking of metallic glass plates in bending, Journal of Applied Physics. 94 (2003) 904-911.

[53] R.D. Conner, Y. Li, W.D. Nix, and W.L. Johnson, Shear band spacing under bending of Zr-based metallic glass plates, Acta Materialia. 52 (2004) 2429-2434.

[54] D.C. Hofmann, J.Y. Suh, A. Wiest, G. Duan, M.L. Lind, M.D. Demetriou, and W.L. Johnson, Designing metallic glass matrix composites with high toughness and tensile ductility, Nature. 451 (2008) 1085-9.

[55] C.Q. Chen, Y.T. Pei, and J.T.M. De Hosson, Effects of size on the mechanical response of metallic glasses investigated through in situ TEM bending and compression experiments, Acta Materialia. 58 (2010) 189-200.

[56] X.W. Gu, and J.R. Greer, Ultra-strong architected Cu meso-lattices, Extreme Mechanics Letters. 2 (2015) 7-14.
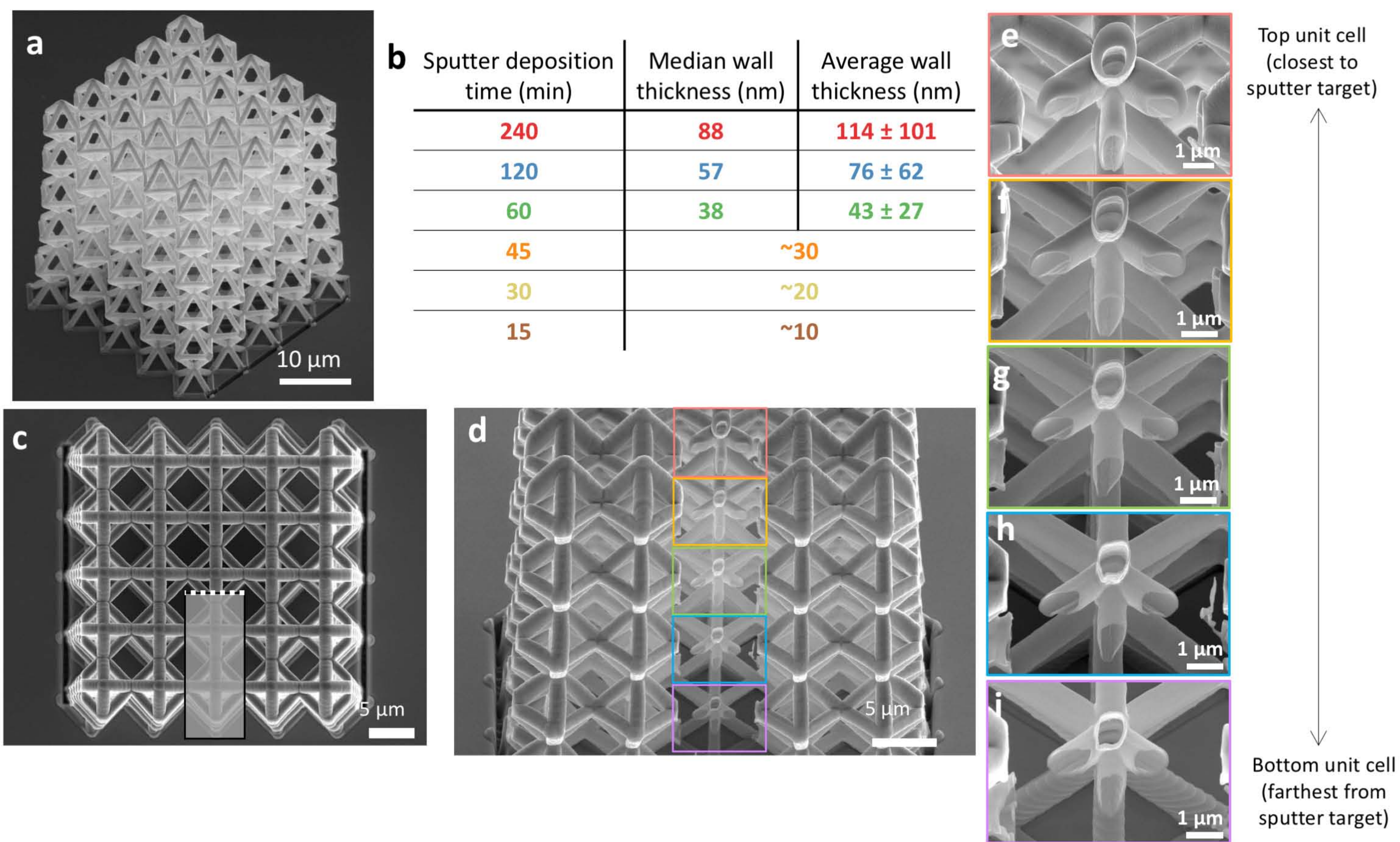
Figure 1. Nanolattice geometry and wall thickness. (a) SEM image of a nanolattice taken at 50° stage tilt. The sputter deposition used to fabricate the nanolattices resulted in significant variation in metallic glass wall thickness as indicated in table (b) which notes the median and average wall thicknesses ± one standard deviation for the different sputter deposition times. Sputter deposition times of 45 minutes and less resulted in nanolattice beams with walls too thin to reliably measure, hence the wall thicknesses for those deposition times are estimated. (c) Top-down image of a nanolattice fabricated by sputter deposition for 240 minutes with rectangle denoting the region removed by FIB to expose the cross-sectional SEM images shown in (d-i). The images in (e-i) are higher magnification images of the unit cells in (d) arranged in top-down order with (e) the top unit cell and (i) the bottom unit cell.
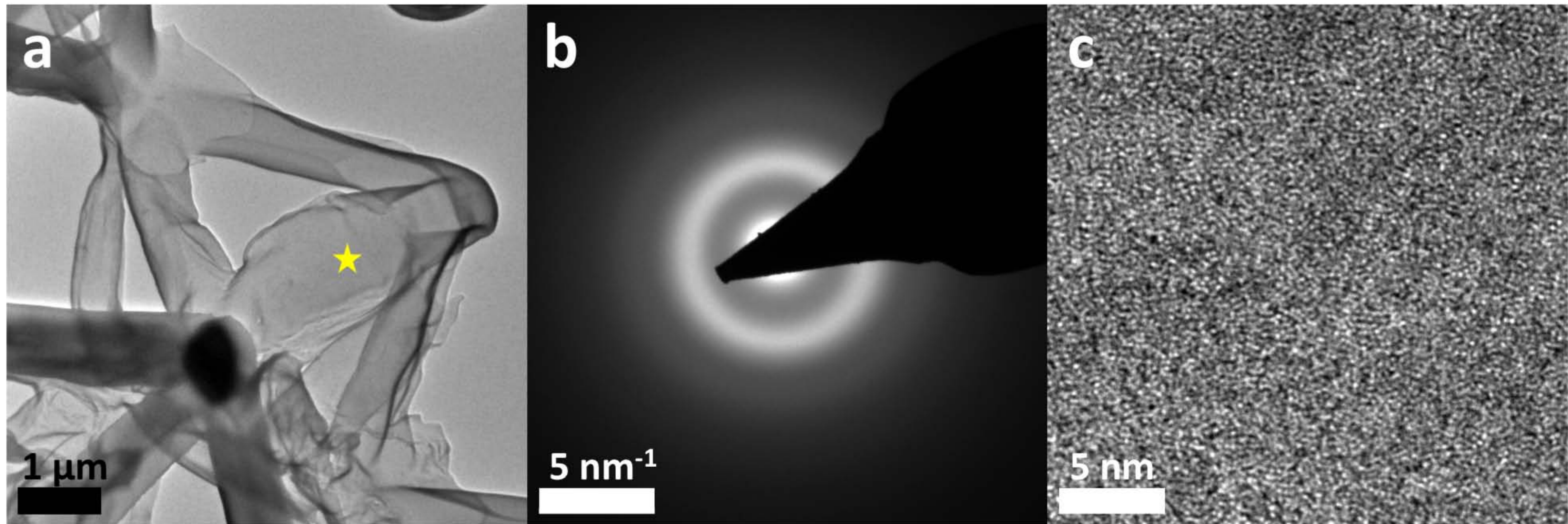
Figure 2. Microstructural analysis by TEM performed on a section of a Zr-Ni-Al nanolattice. (a) TEM image of a particular unit cell in that nanolattice. The (b) diffraction pattern and (c) high resolution TEM image were obtained from the region centered around the yellow star marked in (a).
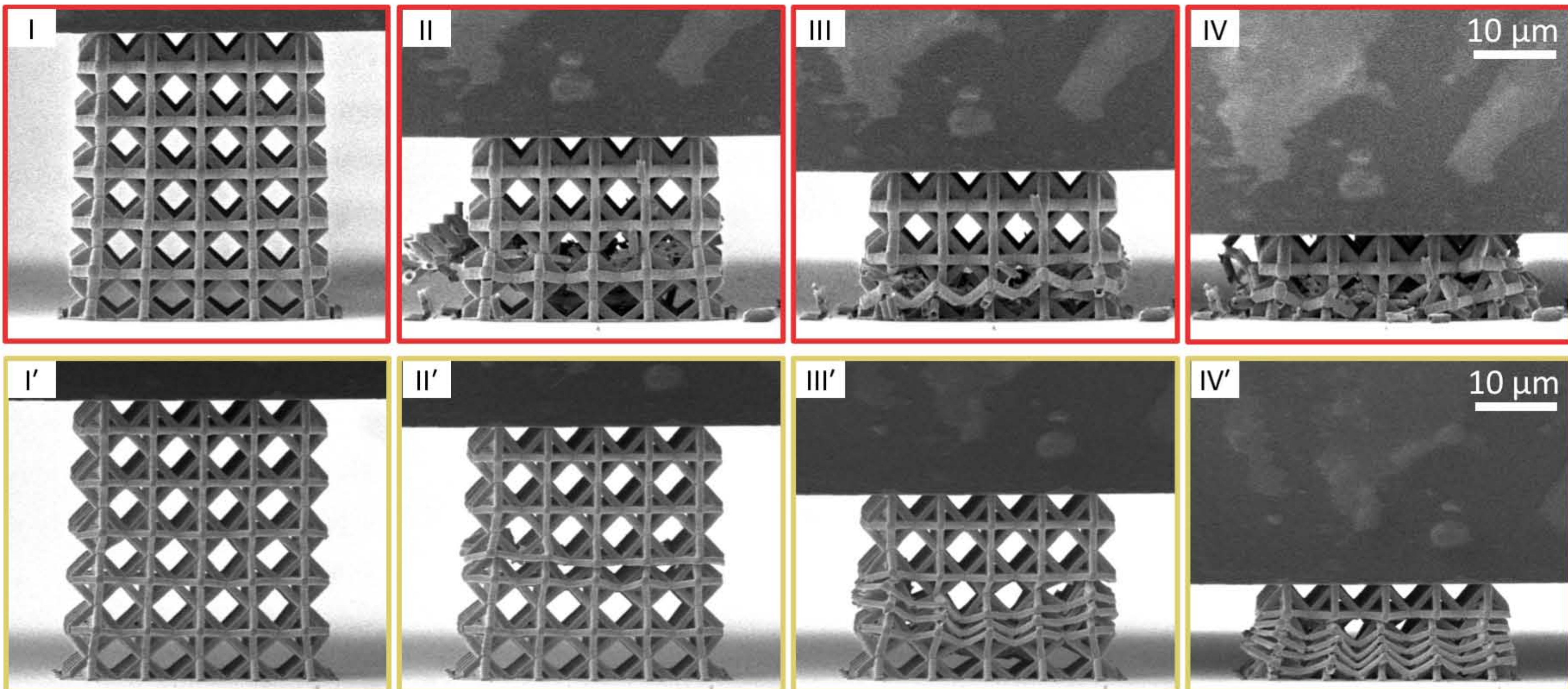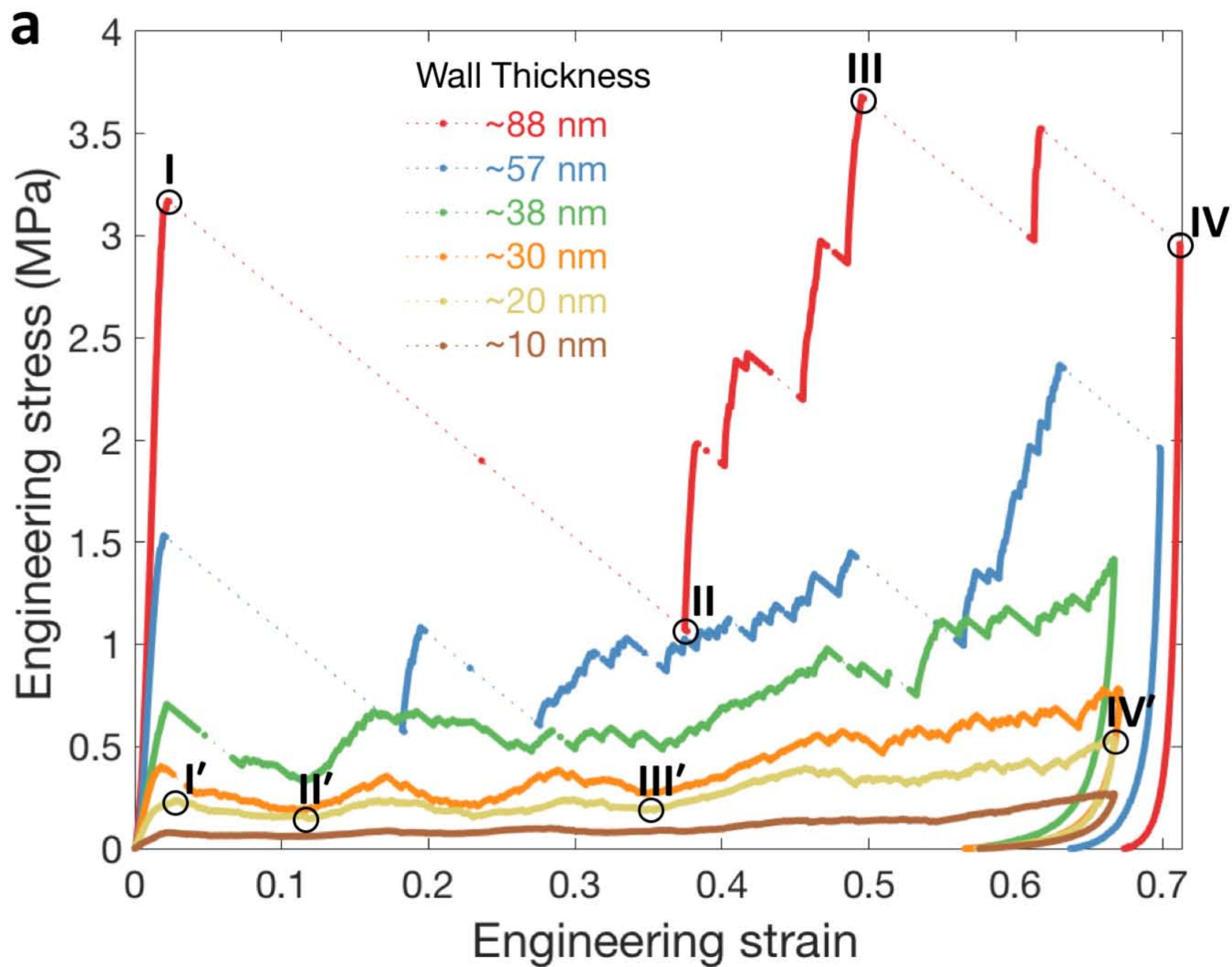
Figure 3. Representative engineering stress-strain data obtained via uniaxial compression to ~67% strain. One representative stress-strain curve for each wall thickness is shown in (a) with data points connected with dotted lines. In-situ images obtained during compression at the points marked in (a) are shown in (I-IV) for the nanolattice with a wall thickness ~88 nm and in (I'-IV') for the nanolattice with a wall thickness ~20 nm.
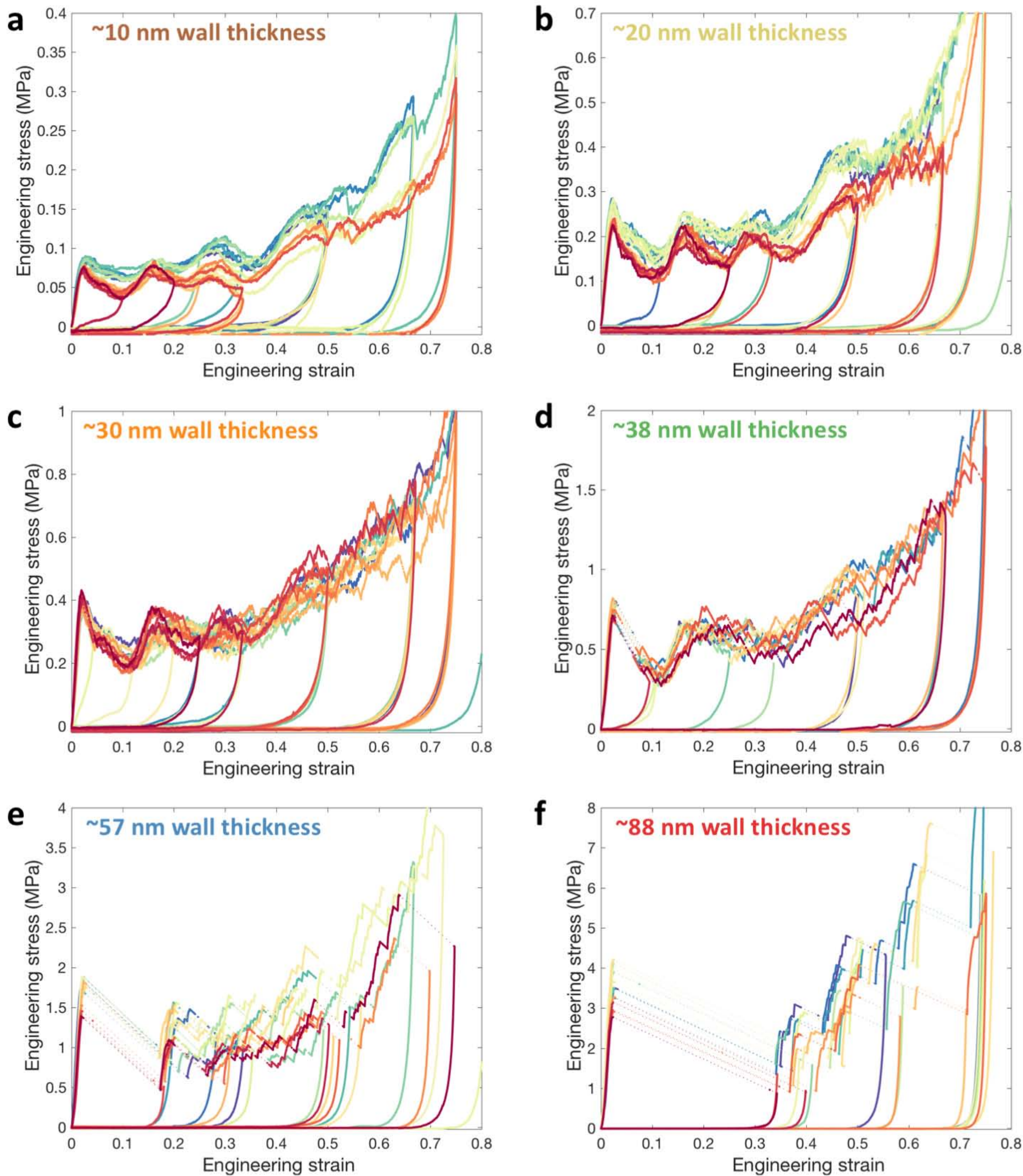
Figure 4. Stress-strain data grouped by nanolattice wall thickness, under compression to a range of strains. The wall thickness of the nanolattice beams for each grouping are (a) 10 nm, (b) 20 nm, (c) 30 nm, (d) 38 nm, (e) 57 nm, and (f) 88 nm. Data points are connected with dotted lines.
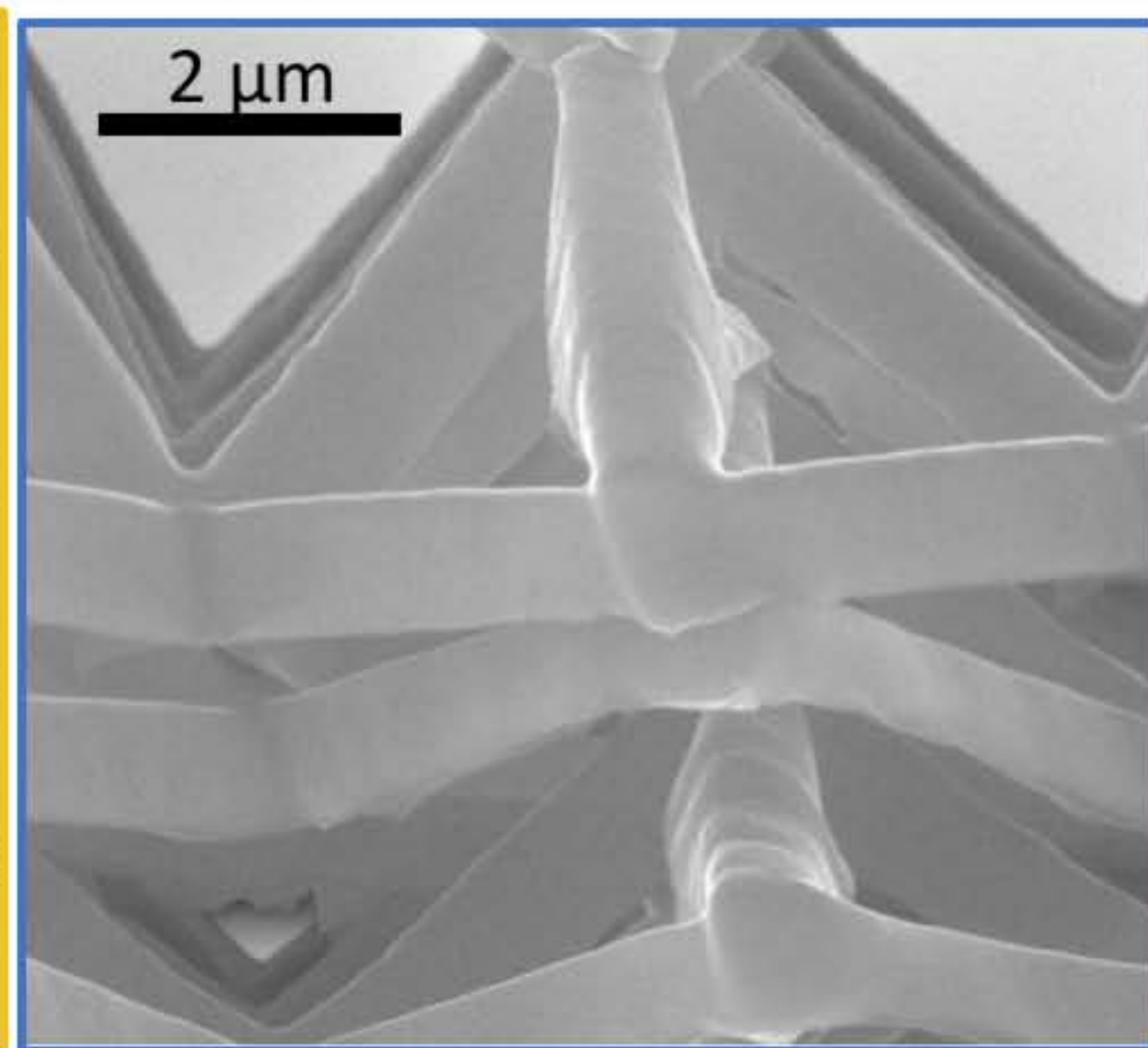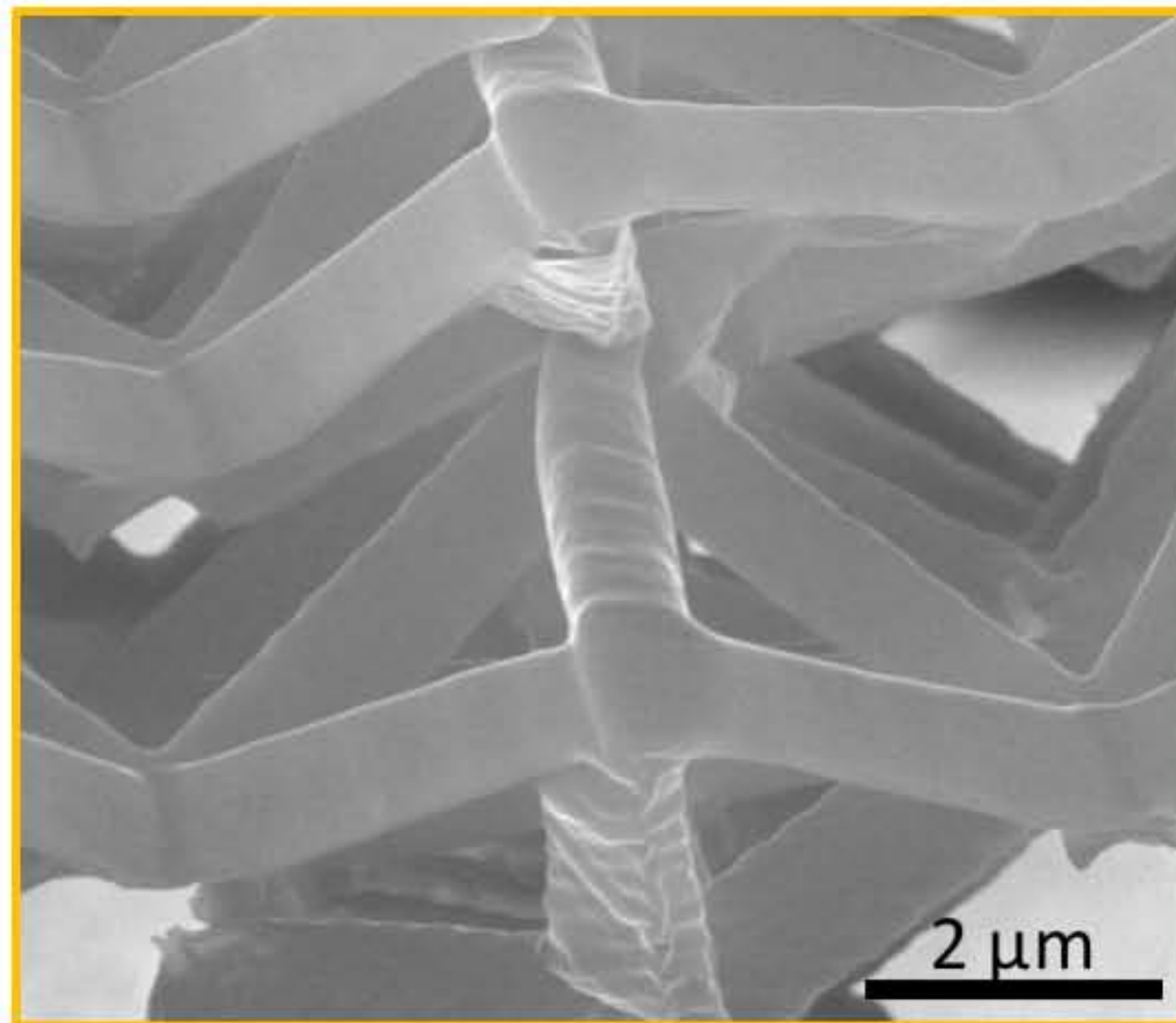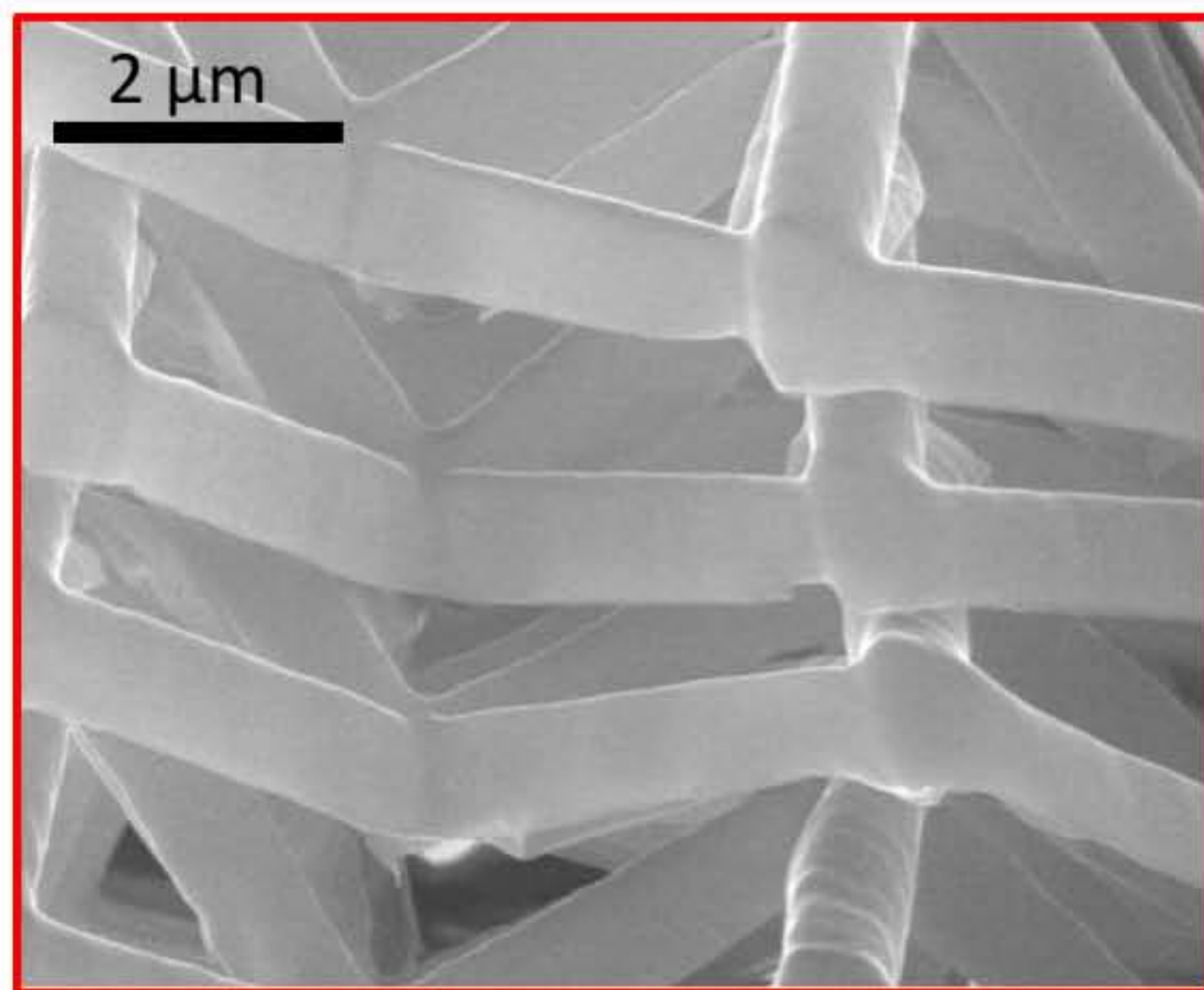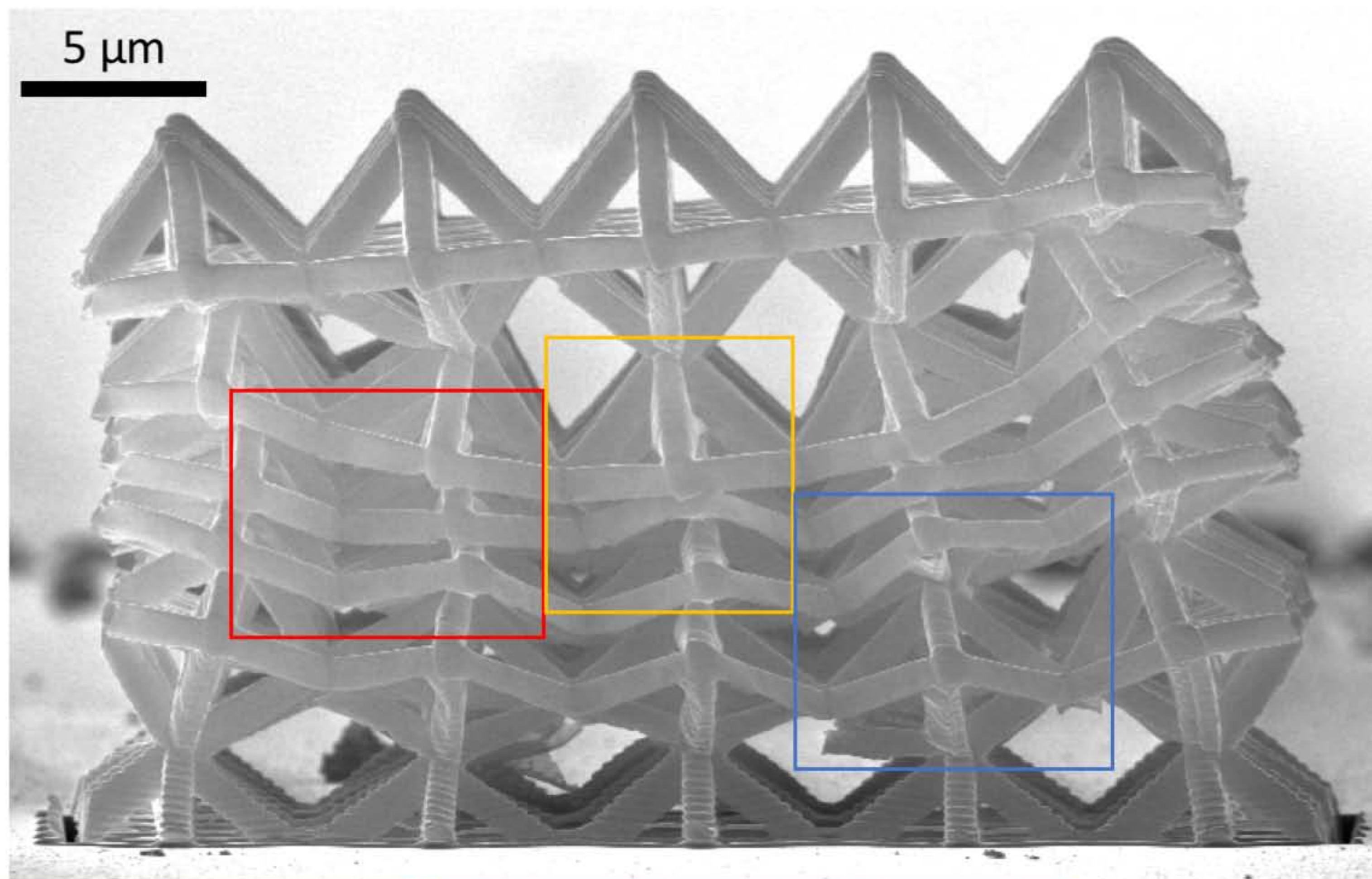
Figure 5. SEM images of a nanolattice with a ~10 nm wall thickness after compression to 67% strain. The colored rectangles in the top image denote the regions for the higher magnification images below. The nanolattice exhibited gradual layer-by-layer collapse during compression.
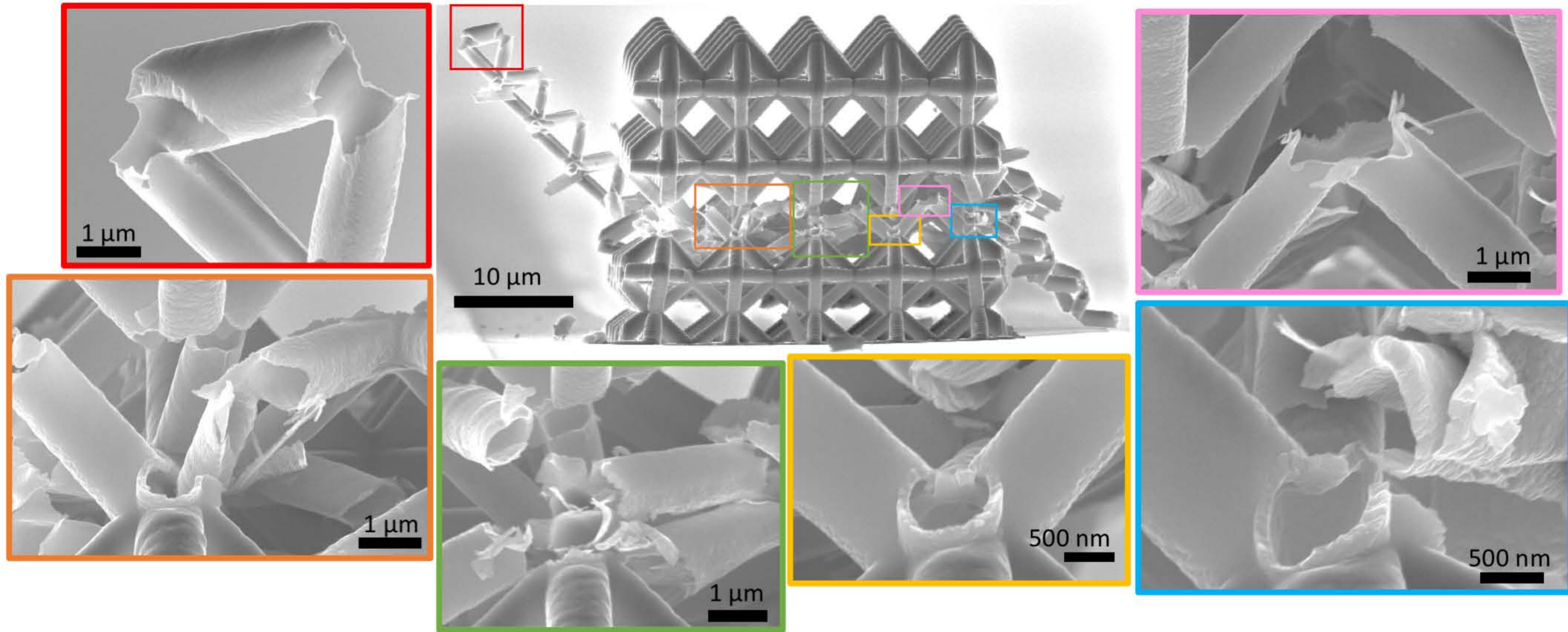
Figure 6. SEM images of a nanolattice with a ~88 nm wall thickness after compression to 33% strain. The colored rectangles in the top-middle image denote the regions for the surrounding higher magnification images. Failure is localized to the two rows of unit cells near the middle of the nanolattice and primarily occurs at the nodes. The failed layers are destroyed and largely unrecognizable after compression.
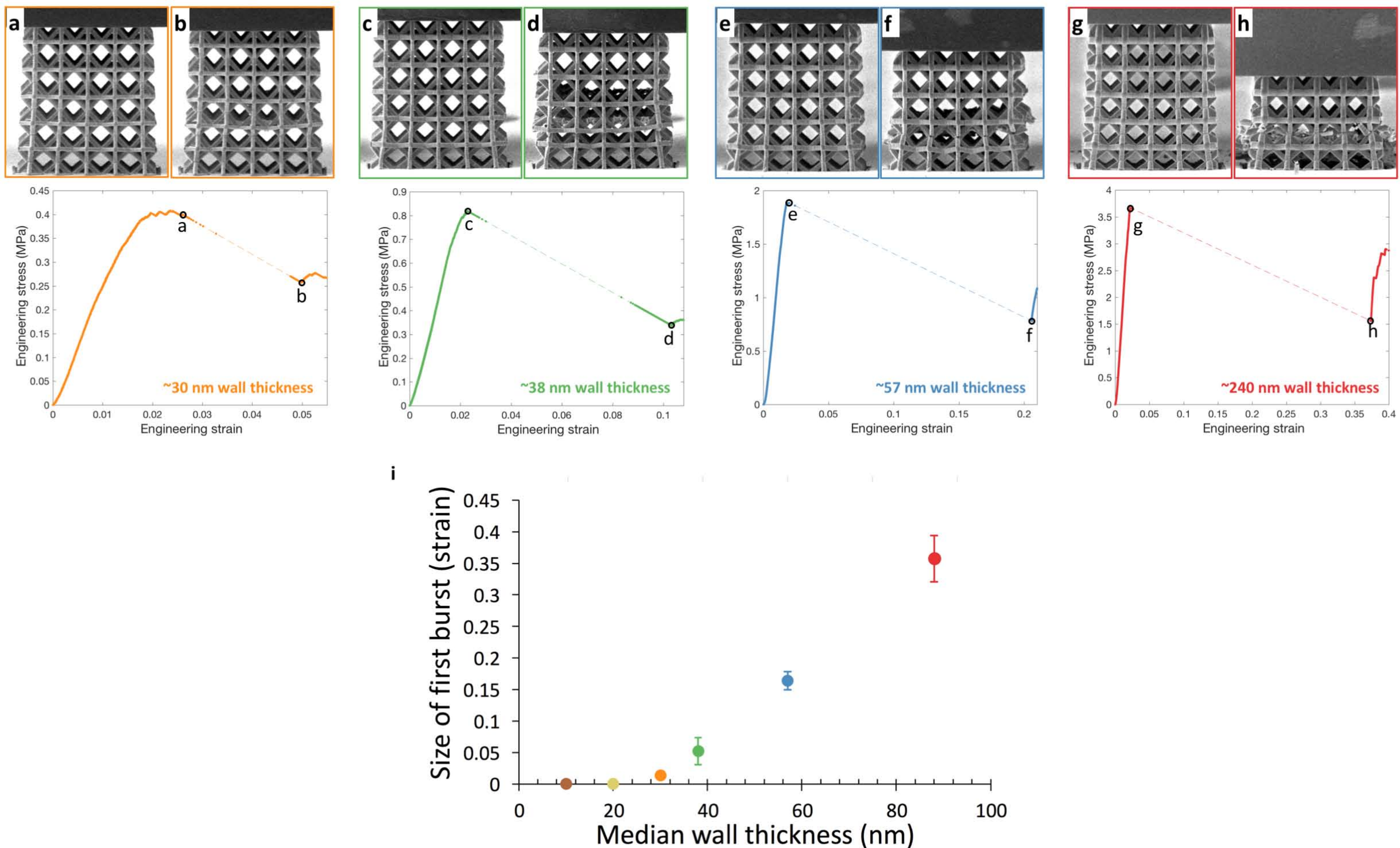
Figure 7. First failure event as a function of nanolattice wall thickness. Following elastic deformation, thicker-walled nanolattices (~30 nm wall thickness and larger) each exhibit a pronounced strain bursts. (a-h) SEM images of first failure events and the corresponding stress-strain data shown below the images for median wall thicknesses of (a, b) ~30 nm, (c, d) ~38 nm, (e, f) ~57 nm, and (g, h) ~88 nm. The size of the strain burst was measured for at least 16 nanolattices of each wall thickness. (i) Average strain burst size as a function of wall thickness with the error bars denoting ± one standard deviation in each measurement.
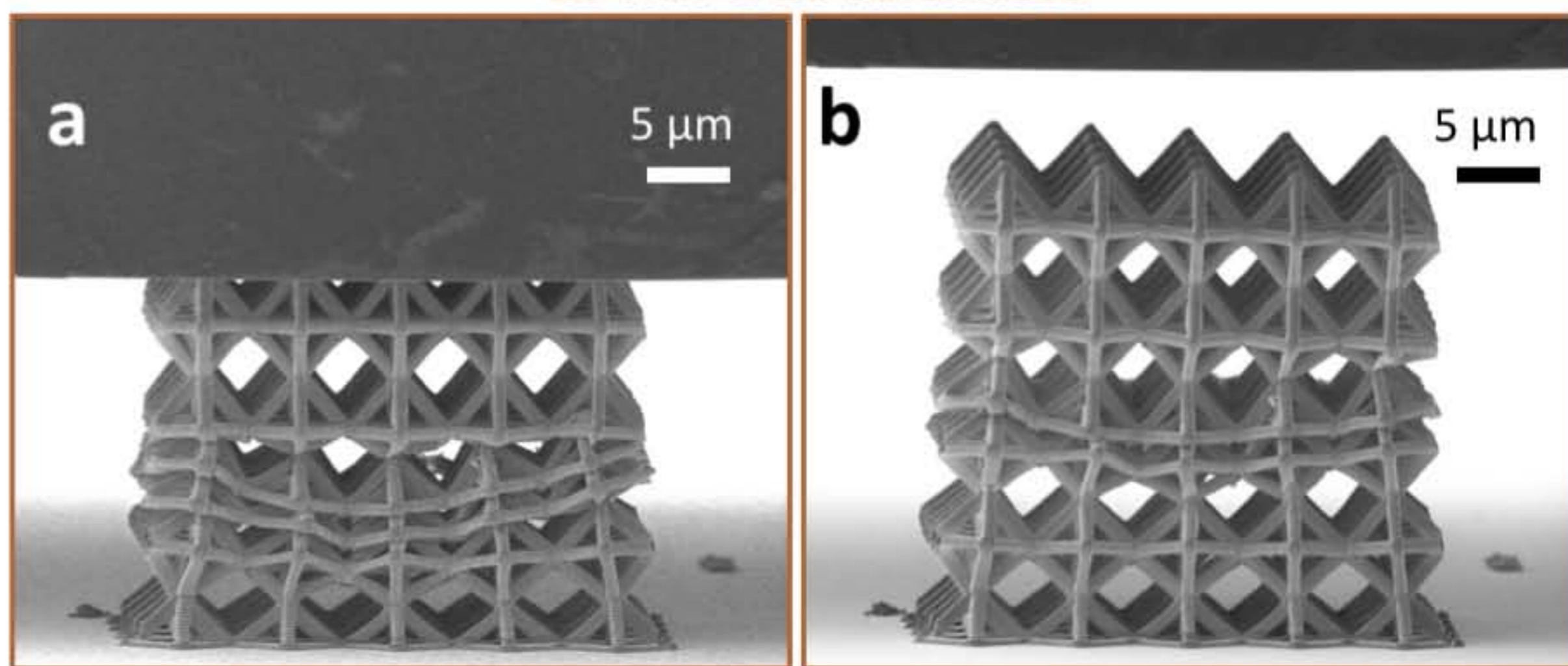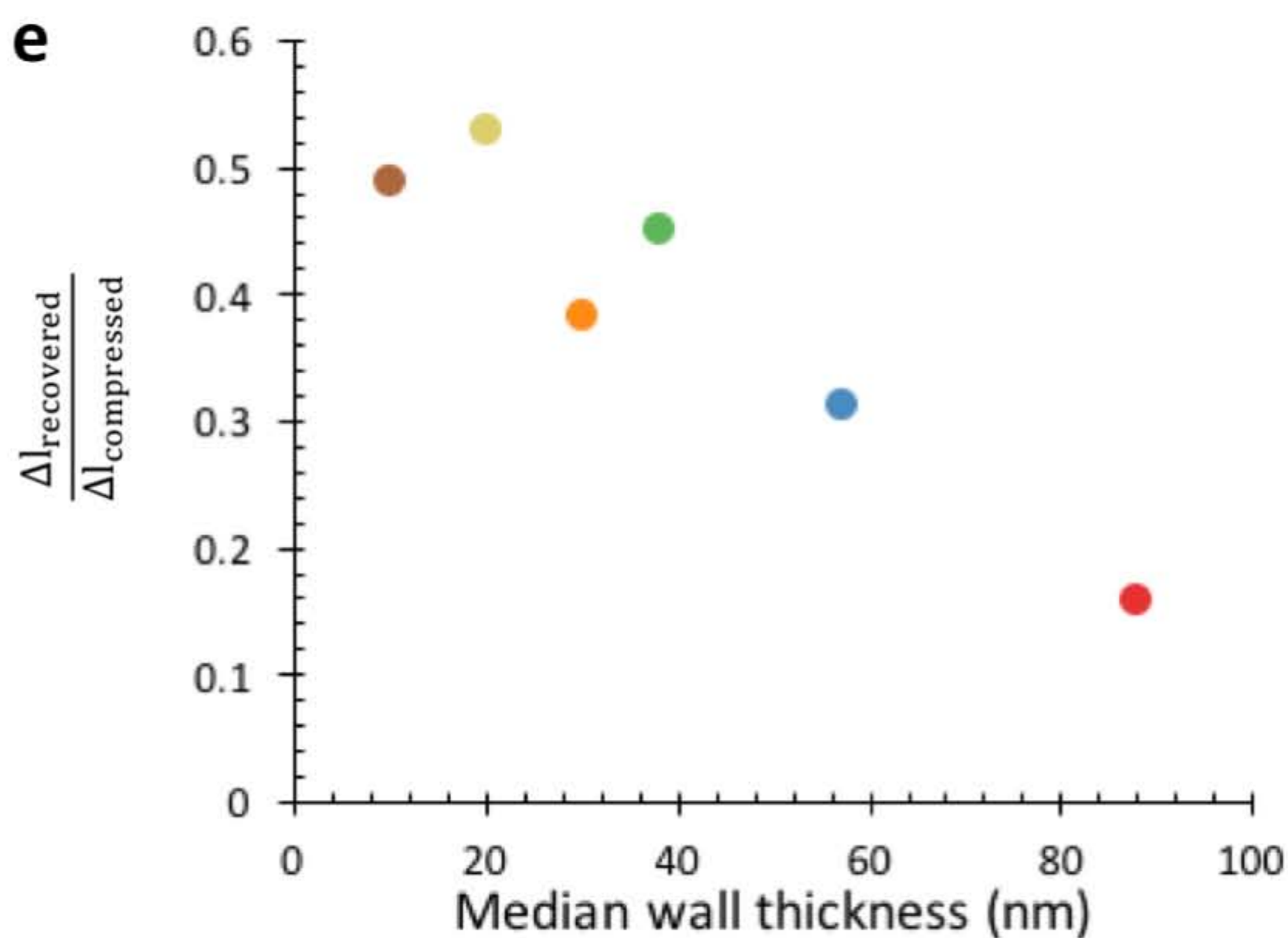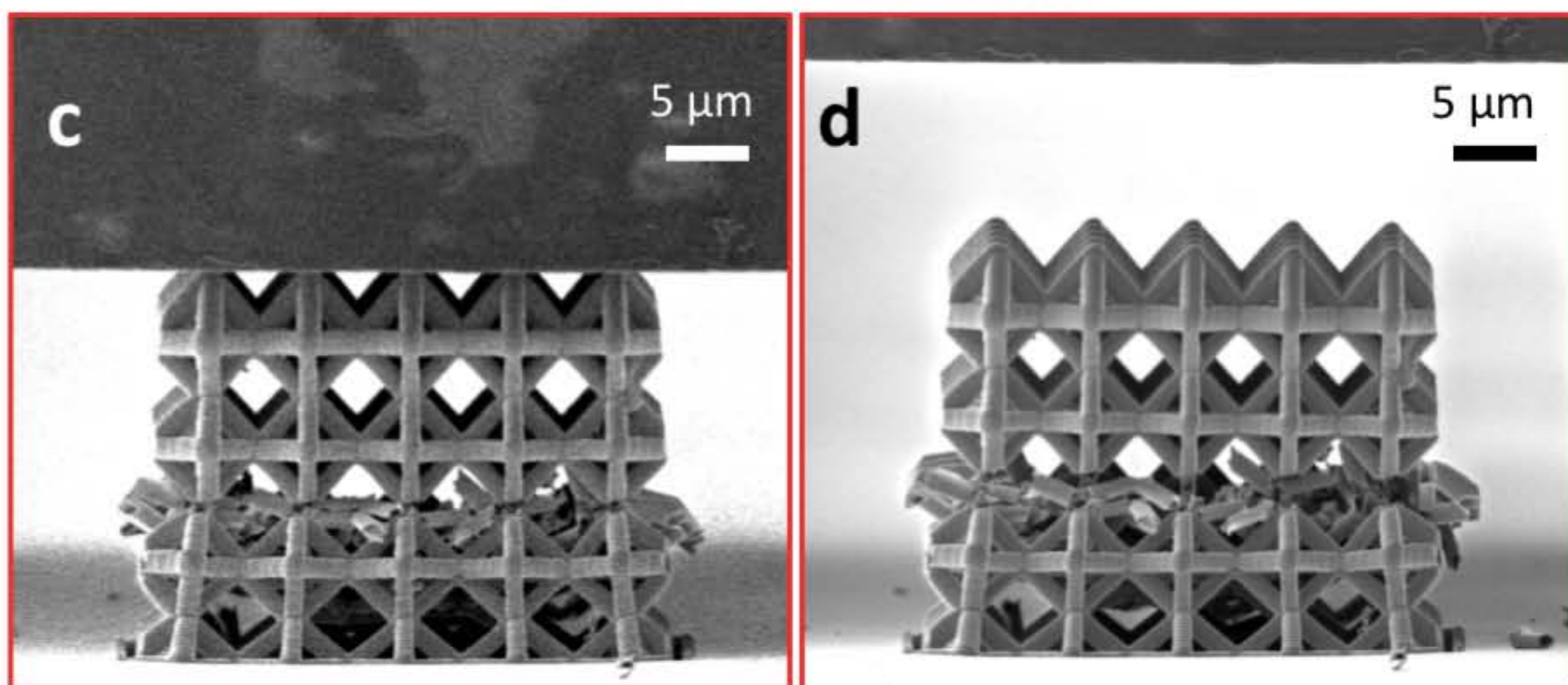
Figure 8. Nanolattice recovery after compression to 33% strain. SEM images shown for nanolattices with a wall thickness of (a, b) ~10 nm and (c, d) ~88 nm. The left images (a) and (c) show the nanolattices at the maximum strain of the compression experiment (~33%) just before unloading. The right images (b) and (d) show the nanolattices immediately after the compression experiment. (e) Plot of recovered height normalized by the compression distance for nanolattices compressed to 33% strain.
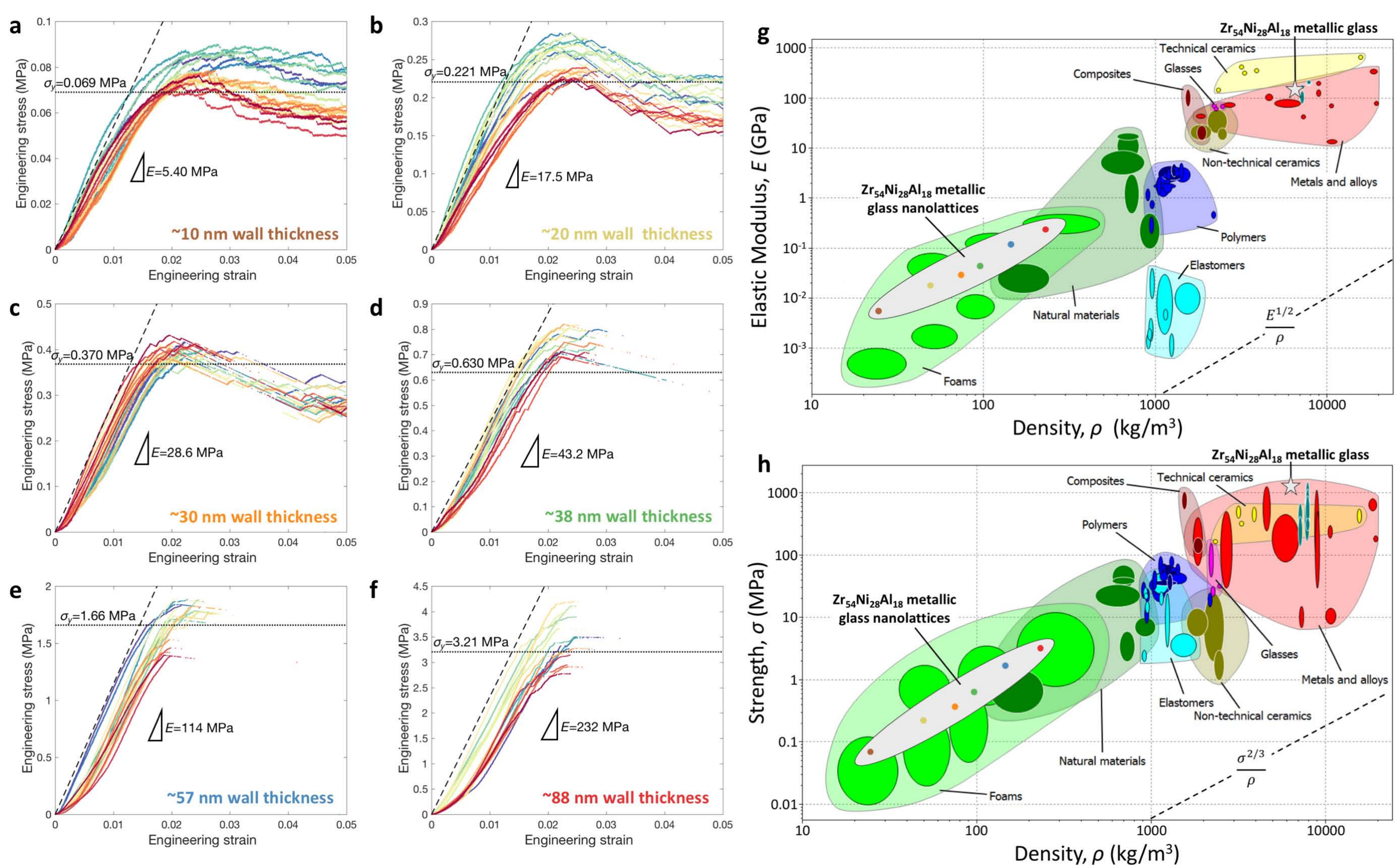
Figure 9. Elastic modulus and yield strength of the nanolattices. (a-f) Engineering stress-strain data displayed from 0-0.05 strain, grouped by wall thickness with (a) 10 nm, (b) 20 nm, (c) 30 nm, (d) 38 nm, (e) 57 nm, and (f) 88 nm. The horizontal dotted lines indicate the average yield strength and the slope of the dashed lines indicate the average elastic modulus for each wall thickness. The presence of large strain bursts in the thicker-walled nanolattices of (d-f) results in large stretches of strain with no data captured, and hence the data appears to cut off at ~0.03 strain. Material property plots of (g) elastic modulus and (h) strength versus density for existing materials. The hollow metallic glass nanolattices are shown in the gray oval with each point corresponding to the average measured property from all the nanolattices of a particular wall thickness. The directional nature of sputter deposition makes the density values unreliable and should thus only be taken as approximate.

Appendix A

Brittle-to-deformable transition in metallic glass nanolattices via decreased wall thickness

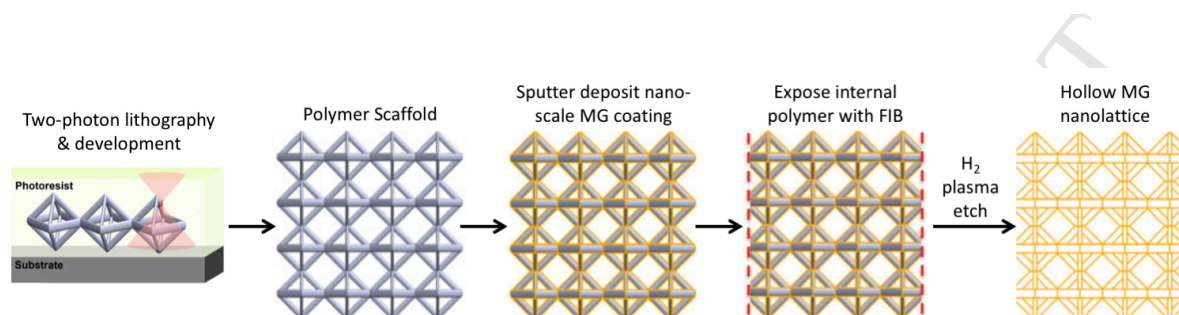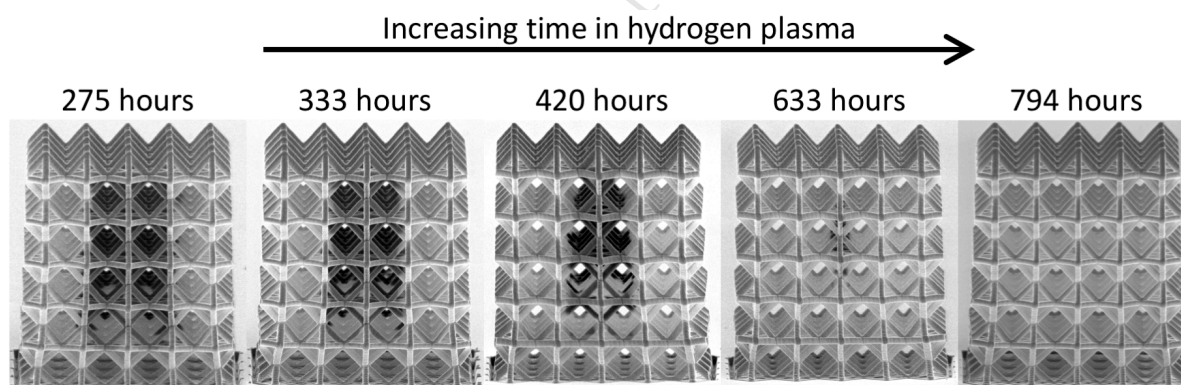*Rachel Liontas and Julia R. Greer*

Figure A1. Fabrication of hollow metallic glass (MG) nanolattices. Fabrication involves utilizing two-photon lithography to write a polymer scaffold which is coated with a nanoscale thickness of metallic glass by sputter deposition. Then FIB is used to remove the outside edges of the metallic glass coating, which exposes the internal polymer scaffold so that it can be subsequently etched away by hydrogen plasma. This process results in a nanolattice structure composed of hollow beams of metallic glass, where the wall thickness of the beams is on the nanoscale.

Figure A2. Nanolattices after various times in hydrogen plasma. The darker region is the un-etched section of metallic glass beams still containing a polymer core and the lighter region is the etched section of hollow metallic glass beams with polymer removed. The etch progression is apparent from the disappearance of the darker region with increased time in hydrogen plasma. Images were taken at ~85° tilt of the SEM stage.
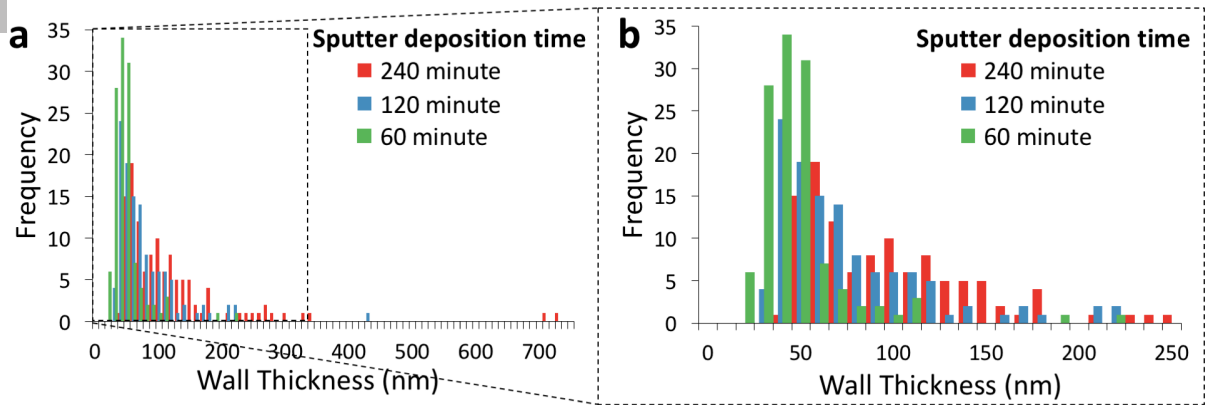
Figure A3. Histogram of wall thickness measurements for nanolattices fabricated by sputter deposition for 240, 120, and 60 minutes. (a) Histogram displayed over the entire range of measured wall thicknesses from 0-750 nm. (b) Histogram zoomed in to the wall thickness range of 0-250 nm to make the distributions at small wall thicknesses more visible. Sputter deposition times of 240, 120, and 60 minutes correspond respectively to nanolattice median wall thicknesses of 88, 57, and 38 nm respectively.
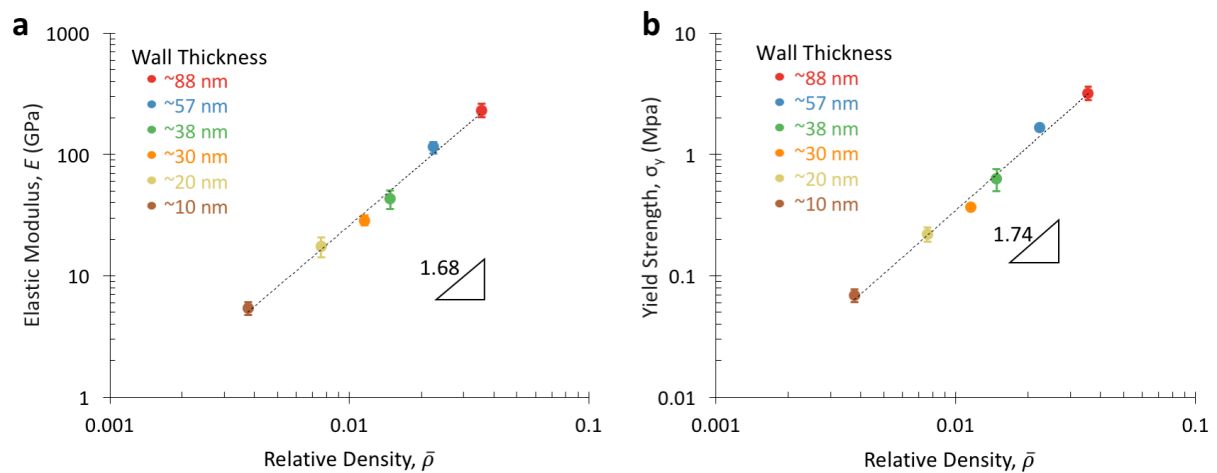

Figure A4. Elastic modulus and strength versus relative density of metallic glass nanolattices. (a) Elastic modulus and (b) yield strength are plotted versus relative density with the error bars denoting ± one standard deviation in the measured property. Due to the logarithmic scales of the plot, some of the error bars are within the marker size and do not appear. The directional nature of sputter deposition makes the relative density values unreliable and should thus only be taken as approximate.

Video 1. Nanolattice with ~10 nm wall thickness compressed to ~67% strain. The video is played back at a speed 50x faster than it was captured.

Video 2. Nanolattice with ~20 nm wall thickness compressed to ~67% strain. The video is played back at a speed 50x faster than it was captured.

Video 3. Nanolattice with ~30 nm wall thickness compressed to ~67% strain. The video is played back at a speed 50x faster than it was captured.

Video 4. Nanolattice with ~38 nm wall thickness compressed to ~67% strain. The video is played back at a speed 50x faster than it was captured.

Video 5. Nanolattice with ~57 nm wall thickness compressed to ~67% strain. The video is played back at a speed 50x faster than it was captured.

Video 6. Nanolattice with ~88 nm wall thickness compressed to ~67% strain. The video is played back at a speed 50x faster than it was captured.